POLITECNICO DI TORINO

Master's Degree in Aerospace Engineering

Politecnico
di Torino

Master's Degree Thesis

Modeling and Control of Docking/Grasping System for a Small Spacecraft

Supervisors

Prof. ELISA CAPELLO

Mr. FABIO FALIERO

Mr. DARIO RUGGIERO

Candidate

MIRKO GIORDANO

April 2023

Abstract

Recently, the use of microsatellites, e.g. CubeSat, has increased due to technology miniaturisation. The combination of several microsatellites allows to design large spacecrafts considering a modular approach and reducing costs. Moreover, in case of a component failure, the modularity makes possible to replace a single spacecraft instead of repairing a larger one. The most critical phase in this concept is the contact among the microsatellites, which is required to be accurate and at low speed, in order to prevent any potential damage. Magnets may reduce design complexity and docking phase during the final approach manoeuvre. The objective of this thesis is the design of a simulator for small satellites docking considering magnets application. Simulation study is carried out in MATLAB/Simulink environment. Magnets with low magnetization are considered such to not interfere with the correct functioning of magnetometers. Moreover, spacecraft attitude is assumed to be stable during the approach manoeuvre in order to have not interaction between magnets and Earth's magnetic field. Magnets are positioned to not generate disturbances interacting with Earth's magnetic field. Position control during the final approach is regulated by an LQR controller, while attitude is regulated by a PD controller. First, the results show that, minimizing the speed in proximity of the docking phase, the magnets are sufficient to operate autonomously the docking manoeuvre. Moreover, the speed reached at the contact point can be easily managed by commonly used materials. After the contact, impact disturbances are considered in the combined system stabilization. The assembled satellite is controlled by the same attitude and position controllers designed for the single spacecraft. These achievements open to the possibility to build simple models to study spacecraft assembly and multiple-docking applications.

Acknowledgements

I would like to express my sincere appreciation to my advisors, Prof. Elisa Capello, Mr. Fabio Faliero, and Mr. Dario Ruggiero for their guidance, encouragement, and unwavering support throughout the research process. I am also grateful to the faculty and staff at Politecnico di Torino for providing me with the resources and opportunities necessary to complete this thesis. To my family and friends, thank you for your love, patience, and support, which have been essential to my success.

Table of Contents

List of Tables

List of Figures

Acronyms

APF Artificial Potential Field

ADCS Attitude Determination and Control System

BRF Body Reference Frame

ECI Earth Centred Inertial

GNC Guidance Navigation and Control

LEO Low Earth Orbit

LQR Linear Quadratic Regulator

LVLH Local Vertical Local Horizontal

PID Proportional-Integral-Derivative

PWPF Pulse-Width/Pulse-Frequency

RW Reaction Wheel

Chapter 1

Introduction

In recent years, technology miniaturization led to a major development in the small satellites field. Research in this field continues to grow due to their cost-effectiveness and versatility. They are used in a wide range of applications such as communication, Earth observation, and scientific research. A new approach to these satellites could be the in-orbit assembly of different units in order to have a larger and more complex structure. This is useful both in terms of cost and design and operation. It would be beneficial from a cost perspective because CubeSats are cheaper to make and launch with respect to a large spacecraft. From the design perspective, CubeSats projects are generally ready to launch in less time than larger spacecraft. On the operation side, this would ease tasks such as assembling, refueling, and maintenance. Moreover, the implementation of permanent magnets would simplify the docking device with respect to the use of electrical magnets and would result in less power consumption. In order to be able to do so, a reliable and accurate docking device is necessary. Permanent magnets could be an interesting solution as they are very simple and do not need to be powered or controlled.

The use of magnetic docking for small satellites has yet to be demonstrated in a practical application, as far as the author is aware. However, various research groups are currently focusing on the advancement of docking technology for small satellites, as indicated by recent studies [1, 2, 3, 4]. Notably, Pei et al. [5, 6] have contributed significantly to the field of magnetic docking through their work. Despite these efforts, the contact between the spacecraft has not been extensively investigated yet, highlighting the need for further research in this area.

The objective of this work is to design a simulator for small satellites docking considering magnets application. By simulating the implementation of a magnetic docking system and evaluating its performance in different scenarios, this works aims to provide a proof of concept for the use of this docking device as an alternative to other possible mechanisms. Additionally, this thesis aims to provide a better understanding of the contact phase and its effects on the assembled spacecraft,

with a particular focus on contact velocity. Contact models are complex and vary depending on the application. In this instance, one of the contact force models described in [7] could be implemented. In particular, the Lankarani-Nikravesh model [8] could have been used, as it is one of the most reliable and widely implemented in multi-body systems. Although these could be valuable alternatives, they would be too specific for the purpose of this thesis. In fact, in this work, the focus is on the impact conditions and their effect on the assembled system. Therefore, as a preliminary approach, the conservation of linear and angular momentum is implemented.

This study contributes to the field of small satellite docking by providing a proof of concept for the use of permanent magnets as a cost-effective, simple, and reliable docking device. By simulating the implementation of a magnetic docking system and evaluating its performance in different scenarios, this work demonstrates the feasibility and potential advantages of using magnets as the sole means of docking for small satellites, providing a valuable alternative to other possible mechanisms. This thesis also provides a contact model for this particular application, considering all the main factors,i.e. the interaction between magnets, the environmental disturbances, and the system's dynamics. The results of this study provide insight into the capabilities and limitations of magnetic docking systems. Additionally, it adds to the possible benefits of combining this docking device with a simple control algorithm, contributing to the ongoing efforts to develop more efficient and effective methods for small satellite docking.

Subsequent to this introduction, the thesis is organized as follows:

- Chapter 2: Mathematical Model
- Chapter 3: Position and Attitude Control Systems
- Chapter 4: Simulation Results
- Conclusions

Chapter 2 presents the mathematical model used for this application. The first section is dedicated to the utilized reference frame, including how to perform the rotation from one to the other. Then, position and attitude kinematics and dynamics are discussed in detail, presenting how they are modeled. Then all the considered environmental disturbances are presented and their model is described. At last, the contact model is thoroughly discussed, presenting the model for magnetic forces and torques. A numerical example is also included to clearly explain how the model works.

Chapter 3 elaborates on the control algorithms utilized for the position and attitude of the system. The chapter commences with a thorough depiction of the actuation system which includes the mathematical models and configuration of

both thrusters and reaction wheels. Subsequently, the chapter describes the control laws applied, which consist of a PID controller for the attitude control system and an LQR controller for position control.

In Chapter 4, the results of this study are presented. Different test cases have been analyzed. First, the simulation of a docking maneuver has been investigated in ideal conditions, i.e. without environmental disturbances. Then, the same maneuver has been simulated in real conditions, therefore adding the disturbances. At last, an approach and dock maneuver has been tested in both real and ideal conditions. The difference with the previous maneuver is that the satellites involved are now further apart and one of them has a position controller.

The Conclusion chapter provides a summary of the results and discusses possible future work and implications based on this thesis.

Chapter 2

Mathematical Model

2.1 Reference frames

Different phases of a spacecraft mission are generally described using different reference frames [9]. These different frames are used in order to have a more intuitive understanding of the spacecraft motion and to simplify calculations that in other reference frames could be complicated. During the launch phase, when the mission's orbital parameters have not yet been achieved, trajectories are represented using an Earth Centered Inertial (ECI) frame. This is because the relative position to the Earth is crucial in the initial phases of the mission. In this thesis, a final approach manoeuvre is analysed. Therefore the reference frames used are the Local Vertical Local Horizontal (LVLH) frame and the Body frame.

2.1.1 LVLH Reference Frame

In spaceflight dynamics, it is essential to have a reference frame that accurately describes the motion and orientation of a spacecraft. The Local Vertical Local Horizontal (LVLH) reference frame, also known as the spacecraft local frame, is a quasi-inertial reference frame commonly used for this purpose. One of the advantages of this reference frame is that it is local, therefore it is defined relative to the spacecraft rather than a fixed point in space. Hence it is ideal for describing the spacecraft movement during complex manoeuvres, because motion can be described as independent from other objects motion in space. Moreover, this reference frame is used in Guidance, Navigation and Control (GNC) systems, because it is simpler to measure and control both spacecraft attitude and position in the LVLH frame. One of the limitations of this reference frame is that it is only valid for spacecraft in low Earth orbit, therefore is not suitable for describing motion in other orbit types or for interplanetary missions. In addition, LVLH frame is not convenient for highly eccentric orbits as it would complicate attitude control and navigation,

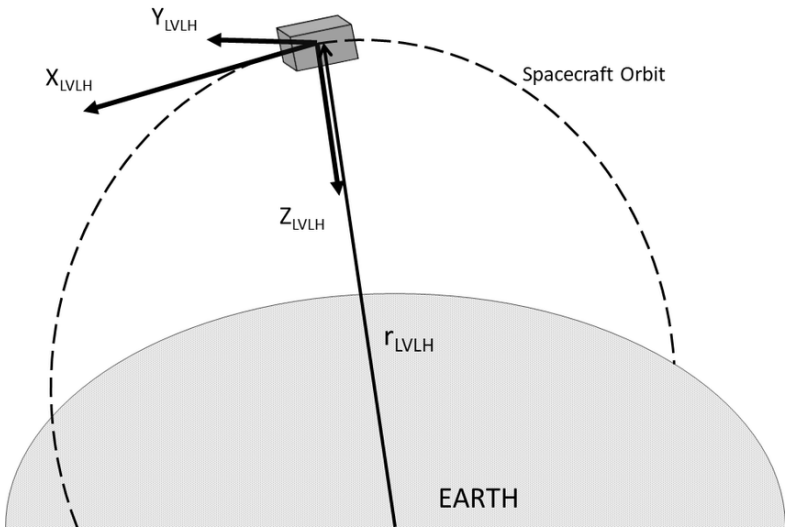

Figure 2.1: LVLH Reference Frame. Adapted from [10].

hence only circular orbits are considered.

As shown in Figure 2.1 the X axis, often called V_{bar}, is aligned with the local horizontal direction of the spacecraft. The Y axis, called H_{bar}, is perpendicular to the orbital plane and it has opposite direction with respect to the angular momentum. The Z axis, R_{bar}, is along the vertical line towards the Earth center, therefore it is NADIR pointing.

2.1.2 Body Reference Frame

The body reference frame (BRF), also known as spacecraft attitude frame, is mostly used for the definition of angular velocity dynamics. It is a non-inertial reference frame fixed to the spacecraft with the origin located at the centre of mass and the frame's axes are oriented along the spacecraft principal axes of inertia. The principal axes of inertia are the directions in which the spacecraft has maximum and minimum moments of inertia. A simple model with its body reference frame is represented in Figure 2.2. The direction with the maximum moment of inertia defines the X-axis, also called the roll axis; the lateral direction defines the Y-axis, called pitch axis, and the vertical direction defines the Z-axis, or yaw axis.

The advantage of this reference frame is that the angular velocity vector of the spacecraft can be expressed directly in terms of the body fixed axis, which makes it easier to design control laws that achieve a desired behavior. All disturbances caused by the space environment are calculated in the body reference frame. While

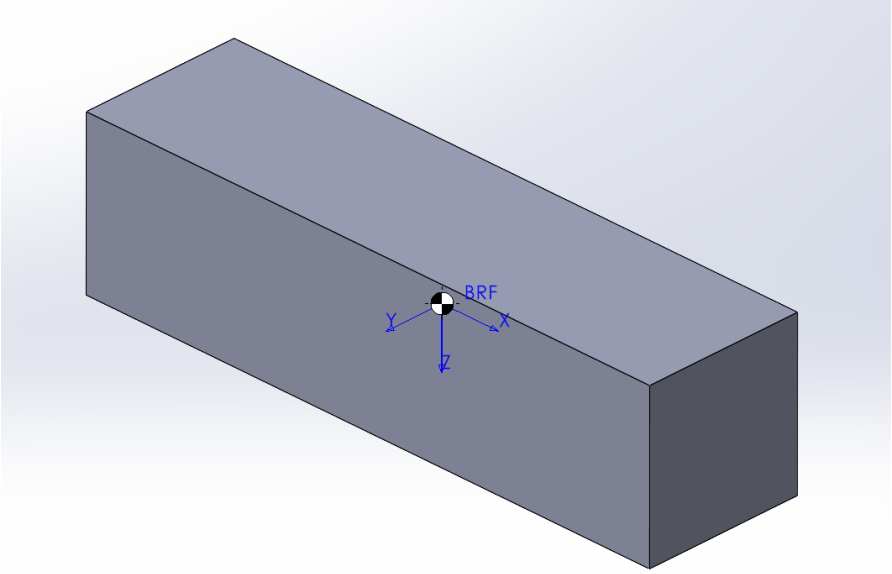

Figure 2.2: Simple example of Body Reference Frame

this coordinate system is particularly useful for determining and controlling attitude, it is important to note that it is not directly applicable to calculate the spacecraft motion. To relate the body reference frame to other reference frames, a rotation matrix must be used.

2.1.3 Rotations between reference frames

In spacecraft dynamics, it is often necessary to switch between different reference frames to analyze and control the motion of the spacecraft. As mentioned before, the body reference frame is useful for describing the attitude of the spacecraft, while the LVLH frame is commonly used for describing the motion of the spacecraft. To switch between these frames, a rotational matrix is used. Rotational matrices are discussed in detail in literature [11]. The rotation between the two reference frames can be performed using Euler angles, which are a set of three angles that specify the orientation of a rigid body in 3D space with respect to a fixed coordinate system. The Tait-Bryan rotation (3-2-1) is used to pass from BRF to LVLH. Adopting this convention, the three rotations in sequence are:

1. the first rotation is about the Z-axis by an angle ψ to align the X_b axis with the LVLH X axis.

The rotational matrix can be expressed as:

$$[\Psi] = \begin{bmatrix} \cos\psi & -\sin\psi & 0 \\ \sin\psi & \cos\psi & 0 \\ 0 & 0 & 1 \end{bmatrix} \tag{2.1}$$

2. the second rotation is about the new Y_b axis by an angle θ to align the Z_b axis with the LVLH Z axis.
   The rotational matrix can be expressed as:

$$[\Theta] = \begin{bmatrix} \cos\theta & 0 & \sin\theta \\ 0 & 1 & 0 \\ -\sin\theta & 0 & \cos\theta \end{bmatrix} \tag{2.2}$$

3. the third and final rotation is about the new X_b axis by an angle ϕ to align the Y_b axis with the LVLH Y axis.
   The rotational matrix can be represented as follows:

$$[\Phi] = \begin{bmatrix} 1 & 0 & 0 \\ 0 & \cos\phi & -\sin\phi \\ 0 & \sin\phi & \cos\phi \end{bmatrix} \tag{2.3}$$

Multiplying together these three matrices a new matrix is obtained:

$$L_{IB} = [\Psi] \cdot [\Theta] \cdot [\Phi] \tag{2.4}$$

Using this new matrix any vector in the body reference frame can be transformed into the LVLH frame by the relation:

$$\vec{r}_{LVLH} = L_{IB} \cdot \vec{r}_B \tag{2.5}$$

Using Euler angles rotations is intuitive because they represent three physical rotations, therefore can be easily visualized. This approach, while it seems convenient, could lead to the gimbal lock phenomenon. It occurs when one of the rotational axes becomes aligned with another, resulting in a loss of one degree of freedom. It happens when the second rotation in a sequence of three rotations aligns with the first or the third rotation.To avoid gimbal lock, attitude representation with quaternions is adopted. This representation and its use will be addressed in the next section of this chapter.

2.2 Position and Attitude dynamics and kinematics

Position and attitude dynamics and kinematics are fundamental parts of the mathematical modeling of spacecraft motion, both in terms of position and orientation.

A detailed description of both can be found in literature [11]. A more specific model similar to the one utilized here, can be found in [12]. Attitude kinematics is concerned with describing how an object's orientation changes over time, without considering the forces that cause the motion. Attitude dynamics, on the other hand, takes into account the forces and torques acting on a spacecraft that cause its attitude to change. It is important as it allows to predict and control the attitude of a spacecraft under different conditions. Position kinematics deals with the relationships between position, velocity, and acceleration of a spacecraft, without considering the forces acting on it. Position dynamics has to account for forces like the ones provided by thrusters and external disturbances. It is described by equations that include the forces acting on the object and how they change its velocity and acceleration over time. The subsections that follow will explore in detail the kinematic and dynamic aspects of spacecraft motion.

2.2.1 Attitude kinematics

Supposing to perform the rotations analyzed in the previous chapter, we can call the starting reference frame F_2, the desired reference frame F_1, and the intermediate reference frames resulting from the first and second rotation F_2' and F_2'' respectively. F_2 is described by the unit vectors (l, m, n) and F_1 by the unit vectors (i, j, k). For the kinematic equation, we have:

$$(\dot{\psi}, \dot{\theta}, \dot{\phi}) = f(\omega_{x_1}, \omega_{y_1}, \omega_{z_1}, \phi, \theta, \psi) \implies \omega_r = \dot{\psi}n + \dot{\theta}m' + \dot{\phi}i \tag{2.6}$$

where $\dot{\psi}, \dot{\theta}, \dot{\phi}$ are the derivatives of Euler angles and represent:

- $\dot{\psi}$ =angular velocity of F_2' referred to F_2
- $\dot{\theta}$ =angular velocity of F_2'' referred to F_2'
- $\dot{\phi}$ =angular velocity of F_1 referred to F_2''

The goal is to express the ω_r vector in F_1. In order to do so it is necessary to calculate the angular velocity of F_2' referred to F_1 as

$$\dot{\Psi}_1 = [\Phi]^{-1}[\Theta]^{-1}\dot{\Psi}_{2'}, \text{ where } \dot{\Psi}_{2'} = \dot{\psi}n \tag{2.7}$$

and the angular velocity of F_2'' referred to F_1 as

$$\dot{\Theta}_1 = [\Phi]^{-1}\dot{\Theta}_{2''}, \text{ where } \dot{\Theta}_{2''} = \dot{\theta}m' \tag{2.8}$$

Therefore, substituting in equation (2.6), the following expression is obtained:

$$\omega_r = [\Phi]^{-1}[\Theta]^{-1}\dot{\psi}n + [\Phi]^{-1}\dot{\theta}m' + \dot{\phi}i \tag{2.9}$$

which can be written as:

$$\omega_r = \begin{bmatrix}\omega_{x1}\\ \omega_{y1}\\ \omega_{z1}\end{bmatrix} = \begin{bmatrix}1 & 0 & -sin\theta\\ 0 & cos\phi & sin\phi cos\theta\\ 0 & -sin\phi & cos\phi cos\theta\end{bmatrix}\begin{bmatrix}\dot{\psi}\\ \dot{\theta}\\ \dot{\phi}\end{bmatrix} \tag{2.10}$$

With the equation in this form, isolating the derivatives of Euler angles allows to write the kinematics equation:

$$\begin{bmatrix}\dot{\psi}\\ \dot{\theta}\\ \dot{\phi}\end{bmatrix} = \frac{1}{cos\theta}\begin{bmatrix}cos\theta & sin\phi sin\theta & cos\phi sin\theta\\ 0 & cos\phi cos\theta & -sin\phi cos\theta\\ 0 & sin\phi & cos\phi\end{bmatrix}\begin{bmatrix}\omega_{x1}\\ \omega_{y1}\\ \omega_{z1}\end{bmatrix} \tag{2.11}$$

In equation (2.11) is clear how, for a Tait-Bryan rotation (3-2-1), for $cos\theta = 0$ there is a singularity. This is called gimbal lock.
To avoid the problem that this may cause, a representation of spacecraft attitude is used. Based on Euler's theorem, the following 4 Euler parameters, called **quaternions**, can be used to describe a rotation of an angle α about an axis defined by a unit vector $\boldsymbol{a} = a_1\hat{i} + a_2\hat{j} + a_3\hat{k}$:

$$q_0 = cos\frac{\alpha}{2};$$

$$q_1 = a_1 sin\frac{\alpha}{2};$$

$$q_2 = a_2 sin\frac{\alpha}{2};$$

$$q_3 = a_3 sin\frac{\alpha}{2};$$

which can be grouped in a scalar component and a vector one:

$$q_0 = cos\frac{\alpha}{2}$$

$$\boldsymbol{q}_v = \boldsymbol{a} sin\frac{\alpha}{2}$$

Using this approach, the rotational matrix can be written as follows

$$\boldsymbol{L}_{21} = (2q_0^2 - 1)\mathbf{1} + 2\boldsymbol{q}_v\boldsymbol{q}_v^T - 2q_0\boldsymbol{q}_v^X \tag{2.12}$$

where $\mathbf{1}$ is the identity matrix and $\boldsymbol{q}_v^X$ is the skew-symmetric quaternion, which is defined as:

$$\boldsymbol{q}_v^X = \begin{bmatrix}0 & -q_3 & q_2\\ q_3 & 0 & -q_1\\ -q_2 & q_1 & 0\end{bmatrix} \tag{2.13}$$

The equation for angular velocity, using quaternions, can then be expressed by:

$$\begin{bmatrix} \boldsymbol{\omega} \\ 0 \end{bmatrix} = \begin{bmatrix} 2(q_0\mathbf{1} - \boldsymbol{q}_v^X) & -\boldsymbol{q}_v \\ \boldsymbol{q}_v^T & q_0 \end{bmatrix} \begin{bmatrix} \dot{\vec{q}}_v \\ \dot{q}_0 \end{bmatrix} \tag{2.14}$$

Where $\boldsymbol{\omega}$ is the angular velocity vector expressed in the body reference frame. Inverting equation (2.14) to find the derivative of the quaternion, the kinematic equation is obtained:

$$\begin{bmatrix} \dot{\vec{q}}_v \\ \dot{q}_0 \end{bmatrix} = \frac{1}{2} \begin{bmatrix} (q_0\mathbf{1} + \boldsymbol{q}_v^X) & \boldsymbol{q}_v \\ -\boldsymbol{q}_v^T & q_0 \end{bmatrix} \begin{bmatrix} \boldsymbol{\omega} \\ 0 \end{bmatrix} \tag{2.15}$$

It is immediately visible that in this case there are no singularities like in the Euler angles approach, therefore this method will be used for computing the attitude kinematics.

2.2.2 Attitude dynamics

To evaluate the attitude dynamics, the body reference frame is considered. Under the assumptions that the spacecraft has 2 planes of symmetry ($I_{xy} = I_{xz} = I_{yz} = 0$) the classical Euler equations have been used:

$$\dot{\omega}_B = I^{-1}(M_B - \omega_B \times (I\omega_B + I_{RW}\omega_{RW})) \tag{2.16}$$

where:

- $\dot{\omega}_B$ is the angular acceleration vector in the body reference frame
- M_B is the total moment acting on the satellite. This vector has to include the moment due to thrusters and reaction wheels, and the external disturbances. Therefore it can be written as

$$\vec{M}_B = Mthr + \Delta M_{ext} + M_{RW};$$

- ω_B is the angular velocity vector in the body reference frame;
- I is the spacecraft inertial tensor which, for principal inertial axes, is diagonal;
- $I_{RW}\omega_{RW}$ is the actuation term, formed respectively by the inertial tensor and the angular velocities of the reaction wheels

From equation (2.16) can be seen that rotational variables do not depend on translational variables, therefore can be decoupled.

2.2.3 Position dynamics

To analyze the position dynamics, the following assumptions have been made:

1. the orbits are circular and in LEO;
2. relative motion: the satellites are not too far from each other;
3. LVLH frame is adopted.

Under these assumptions, Hill's equations have been used:

$$\begin{aligned} -2\omega\dot{z} &= \frac{1}{m_c}F_x \\ \ddot{y} + \omega^2 y &= \frac{1}{m_c}F_y \\ \ddot{z} + 2\omega\dot{x} - 3\omega^2 z &= \frac{1}{m_c}F_z \end{aligned} \tag{2.17}$$

where:

- $(\ddot{x}, \ddot{y}, \ddot{z})$ are the spacecraft accelerations;
- $(\dot{x}, \dot{y}, \dot{z})$ are the spacecraft velocities;
- (x, y, z) are the spacecraft positions;
- $\omega = \sqrt{\frac{\mu}{r_t^3}}$ is the orbital velocity;
- (F_x, F_y, F_z) are the forces acting on the spacecraft in the LVLH frame.

To be noted is that the equation in X and Z are coupled, therefore a force acting on the X-axis will also cause a change in position in the Z-axis and vice versa. In this case study the satellites are 2. On the approaching one, the forces considered are the ones provided by the thrusters, the magnetic force and the environmental disturbances(both described in a later section). On the non-collaborative spacecraft, only the external force due to the magnets will be considered.

2.3 Environmental disturbances

In space there are no large forces or torques due to the environment, therefore minor influences play a major role in governing position and attitude dynamics of a spacecraft. In this work, the environmental disturbances considered are the aerodynamic drag and the J2 effect that affect the position dynamics. A detailed

description of them can be found in literature [9]. The gravity gradient is inserted in the model as a disturbance that affects attitude dynamics. All environmental disturbances are evaluated in the body reference frame, therefore a rotational matrix needs to be used to pass the disturbances to Hill's equation, as described previously.

2.3.1 Aerodynamic drag

The spacecraft analyzed in this thesis are in LEO, therefore some residual atmosphere needs to be considered. The aerodynamic drag is generated by the remaining atmosphere at the satellite orbit altitude, and can be expressed by:

$$F_D = \frac{1}{2}\rho V^2 S C_D \tag{2.18}$$

where ρ is the atmosphere density; V^2 is the spacecraft orbital velocity; S is the cross section of the satellite and C_D is the drag coefficient. F_D, in first approximation, is modeled as a constant force, therefore all parameters are considered constant. In particular, the density and the drag coefficient are set to: $\rho = 10^{-12}\ kg/m^3$ and $C_D = 2.2$.

2.3.2 J2 effect

The J_i effects are caused by the fact that Earth is not a perfect sphere. They are part of an infinite series mathematical equation that describes the perturbational effects of oblation on the gravity field of a planet. While the series has infinite terms, the J2 is over 1000 times larger than the others and has the strongest perturbing factor on orbits, for this reason it is the only one considered here.
A constant value of the force produced by the J_2 effect is considered for simplicity, since removing its dependence from the instantaneous position of the spacecraft does not affect the order of magnitude of the disturbance. In this case study

$$F_{J_2} = m_c \frac{3 J_2 \mu R_E^2}{2 r^4} \tag{2.19}$$

where:

- m_c is the spacecraft mass;
- $J_2 = 1.08263 \cdot 10^{-6}$ is a constant value;
- $\mu = 3.986 \cdot 10^{14}$ is Earth gravitational parameter;
- R_E is Earth radius in km;

- r is the orbit radius in km

The J2 effect affects only position dynamics, along the three axes, and it is evaluated in the body reference frame.

2.3.3 Gravity gradient

This environmental disturbance affects only the attitude dynamics of the spacecraft. Gravitational torque about the body centre of mass is due to the non-uniformity of the gravitational field in space, and the consequent variations in the specific gravitational force over the spacecraft body. If the gravitational field was uniform, then the centre of mass would be also the centre of gravity, and the gravitational torque about the mass centre would be zero. In order to simplify the evaluation of the gravitational torque, the following assumptions have been made:

a) only one celestial primary body is considered;

b) the primary body has a spherically symmetrical mass distribution;

c) the spacecraft is small with respect to its distance from the centre of mass of the primary body;

d) the spacecraft is made of a single body.

These assumptions are applicable in most spacecraft scenarios. Two are referred to the spacecraft itself and two to the source of the gravitational field.
The torque model used in this work is represented by the following expression:

$$\vec{M}_g = 3 \cdot \omega_0^2 \cdot \hat{r} \times \mathbf{I}\hat{r} \tag{2.20}$$

where:

- $\omega_0 = \sqrt{\frac{\mu}{r^3}}$ is the orbital velocity;
- $\hat{r}$ is the unit position vector in the body reference frame;
- $\mathbf{I}$ is the inertial tensor of the satellite.

2.4 Contact mathematical model

Before modeling the contact itself, a contact detection system needs to be defined. Due to approximation errors in calculating the integrals, the difference in relative position cannot reach 0. Therefore, in this work the contact is considered to have occurred when the relative distance in the X_{LVLH} axis is less than $10^{-4}m$.

The two spacecraft are considered separately until contact is achieved, then they are treated as a single satellite with the combined characteristics of the two CubeSats. Assuming the absence of relevant external forces, the conservation of both angular momentum and linear momentum can accurately model the behavior of two spacecraft in contact. This approach takes into account the complex interactions that occur between spacecraft.
Conservation of linear momentum is expressed by the following equation:

$$m_1\vec{v}_1 + m_2\vec{v}_2 = m_{ac}\vec{v}_{ac} \tag{2.21}$$

where:

- $m_1, \vec{v}_1$ are the mass and the velocity of the first spacecraft, respectively;
- $m_2, \vec{v}_2$ are the mass and the velocity of the second spacecraft, respectively;
- $m_{ac}, \vec{v}_{ac}$ are the mass and the velocity of the assembled spacecraft after the contact occurred.

It is then possible to evaluate the velocity of the spacecraft immediately after contact:

$$\vec{v}_{ac} = \frac{m_1\vec{v}_1 + m_2\vec{v}_2}{m_{ac}} \tag{2.22}$$

Conservation of angular momentum can then be expressed as:

$$I_1\omega_1 + I_2\omega_2 = I_{ac}\omega_{ac} \tag{2.23}$$

where:

- I_1 and ω_1 are the moment of inertia and angular velocity of the first spacecraft, respectively;
- I_2 and ω_2 are the moment of inertia and angular velocity of the second spacecraft, respectively;
- I_{ac} and ω_{ac} are the moment of inertia and angular velocity of the two spacecraft united after contact.

Analog to the linear velocity, the angular velocity right after the contact can be evaluated as:

$$\omega_{ac} = \frac{I_1\omega_1 + I_2\omega_2}{I_{ac}} \tag{2.24}$$

2.4.1 Magnets and magnetic force

As mentioned in the previous chapter, contact between the two spacecraft is achieved through the use of magnets. This section describes the mathematical model for the magnets and the forces and torques generated by their interactions.

Magnets

To simplify calculations, the magnet on the satellites is the same. To design the mathematical model, an approach similar to the one used by Pei et al.[5] has been used. Since the presence of the Earth magnetic field is not taken into account, a single magnet for each spacecraft is considered. As explained in the aforementioned paper, to not interfere with the correct functioning of the magnetometer, it is necessary that the magnetic field at the magnetometer location is less than $0.7\mu T$. The equation for estimating the magnetic field at a given distance is:

$$\vec{B} = \frac{\mu_0}{4\pi}\left[3\frac{(\vec{m}\cdot\hat{r})\hat{r} - \vec{m}}{|r|^3}\right] \tag{2.25}$$

where:

- B is the induced magnetic field;
- $\mu_0 = 4\pi \cdot 10^{-7} H/m$ is the vacuum magnetic permeability constant;
- $\vec{m}$ is the magnetic dipole moment;
- r is the considered distance.

The magnetometer is assumed to be located at $r = 25\ cm$ from the magnet, which is reasonable for the modeled satellites, i.e. 3U CubeSat. Knowing r and the upper limit of B, equation (2.25) can be rewritten to solve for m:

$$\vec{m} = \frac{4\pi}{\mu_0}|r|^3\left[\frac{3}{2}(\vec{B}\cdot\hat{r})\hat{r} - \vec{B}\right] \tag{2.26}$$

The dimension of the magnet is such that it can be located in the space called "tuna can" of the 3U CubeSat. In this application, cylindrical magnets with a $3.2cm$ radius are used. Their height is 3 cm.

Magnetic force and torque

The interaction between magnets produces forces and torques, of which an analytical expression is represented in the aforementioned Pei work. Here these expressions are reported (a and b indexes are indicative of the two different dipoles):

$$\vec{F} = \frac{3\mu_0 m_a m_b}{4\pi|\vec{r}|^4}(\hat{r}(\hat{m}_a\cdot\hat{m}_b) + \hat{m}_a(\hat{r}\cdot\hat{m}_b) + \hat{m}_b(\hat{r}\cdot\hat{m}_a) - 5\hat{r}(\hat{r}\cdot\hat{m}_a)(\hat{r}\cdot\hat{m}_b) \tag{2.27}$$

$$\vec{\tau}_{ab} = \frac{\mu_0 m_a m_b}{4\pi|\vec{r}|^3}(3(\hat{m}_a\cdot\hat{r})(\hat{m}_b\times\hat{r}) + (\hat{m}_a\times\hat{m}_b)) \tag{2.28}$$

Both these equations present a singularity for $r = 0$, i.e. when the two magnets are attached. This is already mitigated by the fact that in this work the contact is considered achieved when relative distance is $< 10^{-4}\ m$, but in the force model the distance is to the power of 4 and this mitigation alone is not enough. When the two magnets are very close to each other, a good approximation of the force between them is given by the expression of the magnetic force between two close surfaces:

$$F = \frac{AB^2}{2\mu_0} \tag{2.29}$$

where:

- A is the surface of the magnet, in this case a circle with radius $r_m = 3.2\ cm$;
- B is the magnetic field. Evaluation of the magnetic field can be complex, to simplify calculations it is here set to constant and equal to the upper bound for the correct functioning of the magnetometer: $B = 0.7\ \mu T$.

The magnetic force is calculated using equation (2.27) it equals the value obtained from equation (2.29), at which point the force is held constant at that value until contact is achieved.

2.4.2 Numerical example

To have proof that the previously exposed concept works, a double integrator has been developed before the orbital simulator. The two spacecraft are here considered as objects in a vacuum, not in orbit. As starting condition, the two spacecraft are aligned with the magnets facing each other. The reference frame is centred at half the distance between the spacecraft, i.e. the contact point. A schematic of the starting condition is represented in Figure 2.3. Magnets are oriented as represented, with the colour green representing the positive magnetic pole and red representing the negative magnetic pole. Therefore an attraction force will be produced by their interaction.

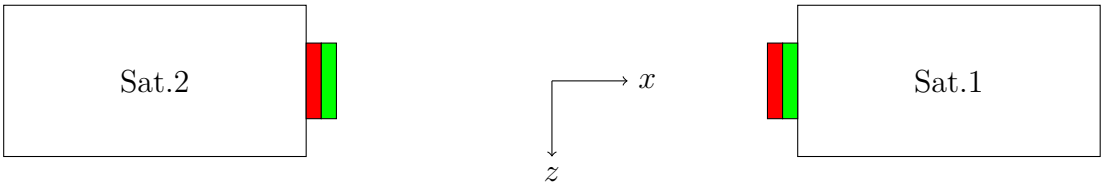

Figure 2.3: Schematic representation of the initial conditions in the double integrator model

	Satellite 1	**Satellite 2**
Dimensions (l_x, l_y, l_z) $[m]$	$(0.1, 0.1, 0.3765)$	$(0.1, 0.1, 0.3765)$
Mass $[kg]$	4	4
Starting position (x_0, y_0, z_0) $[m]$	$(0.1, 0, 0)$	$(-0.1, 0, 0)$
Starting velocity (v_{x0}, v_{y0}, v_{z0}) $[m/s]$	$(0, 0, 0)$	$(0, 0, 0)$

Table 2.1: Characteristics and initial conditions of the two spacecraft in the double integrator model

Their characteristics, along with the initial conditions are listed in Table 2.1. In the following, the results of this simple model are presented.

Double integrator results

In Figure 2.4 the position profiles of the satellites before and after contact are shown. For a clearer representation only the x value is shown because, due to the

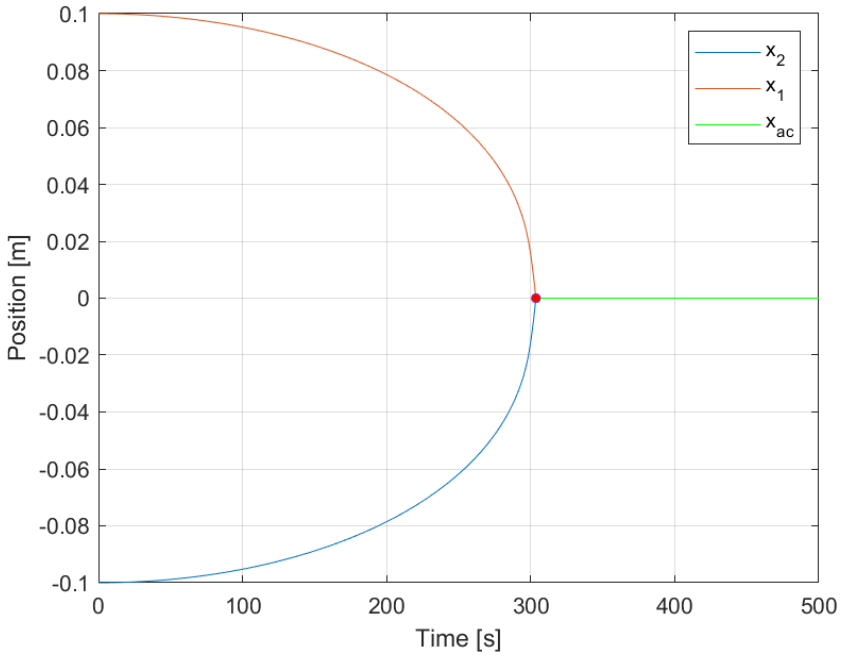

Figure 2.4: Position of the spacecraft before and after contact

absence of external disturbances, the position in y and z is constant and equal to

zero. The contact point is highlighted with a red marker. As can be seen, due to the symmetry of the system, the contact is achieved at the origin of the reference frame.
The satellites velocities are represented in Figure 2.5. Only the x component of the

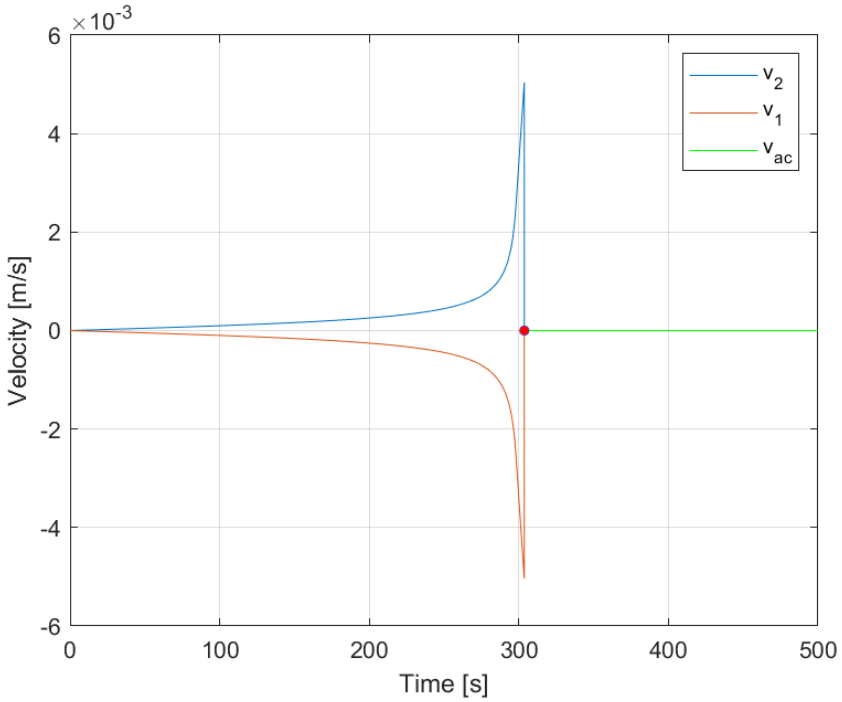

Figure 2.5: Velocity of the spacecraft before and after contact

velocity is shown since the others are null. When contact is achieved, the velocity of the assembled satellite is zero due to the symmetry of the system. Velocity at contact for each satellite is close to $0.5 \cdot 10^{-2}\ m/s$ which is not low. This value will be reduced in the in orbit applications by the use of controllers that will be described as the object of the next chapter.
In this model, angular velocities and magnetic torques are equal to zero throughout all the simulation because the satellites initial configuration is already with the magnets aligned. Due to the absence of external disturbances, this configuration is not perturbed. Therefore the magnetic dipole moments $\vec{m}$ are always parallel and equation (2.28) gives zero as a result.
In Figure 2.6 the applied magnetic force on each satellite is represented. In the graph, it is possible to notice the region where the switch between the two models of the force occurs. In the first phase the force is described by equation (2.27) and right before contact the model is switched to the one presented in equation (2.29) to keep its value constant and avoid the singularity. The magnetic force

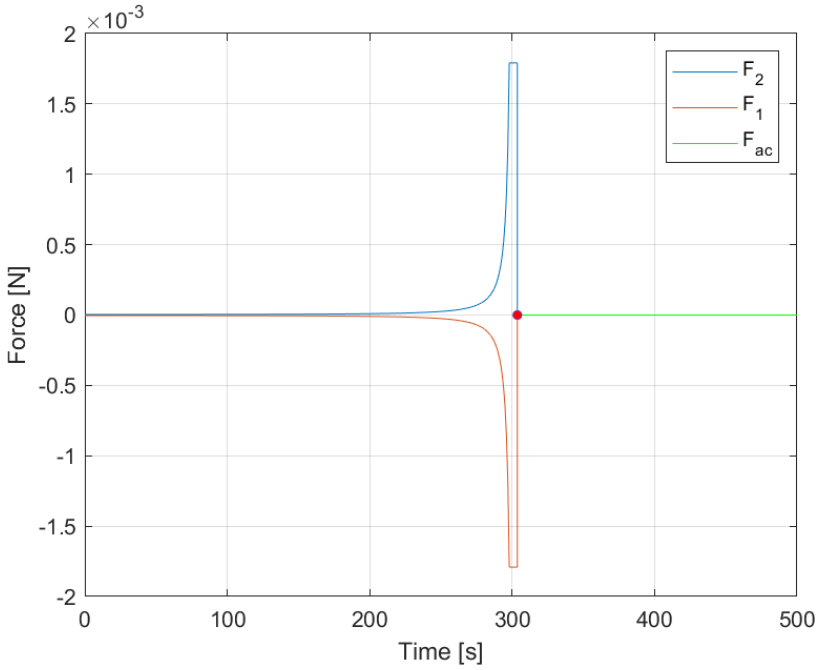

Figure 2.6: Applied Magnetic Force before and after contact

is considered equal to zero after the contact is achieved. This is because when the spacecraft are assembled, the magnetic force ceases to be an external force and becomes internal to the system. To summarize the results, in Table 2.2 the contact conditions of each spacecraft are listed along with the initial conditions of the assembled satellite. This double integrator produced the expected results

	Sat. 1	**Sat. 2**	**After Contact**
Position (x, y, z) $[m]$	$(0, 0, 0)$	$(0, 0, 0)$	$(0, 0, 0)$
Velocity (v_x, v_y, v_z) $[m/s]$	$(-0.005, 0, 0)$	$(0.005, 0, 0)$	$(0, 0, 0)$
Applied Magnetic Force (F_x, F_y, F_z) $[N]$	$(-0.0018, 0, 0)$	$(0.0018, 0, 0)$	$(0, 0, 0)$

Table 2.2: Contact conditions of each spacecraft and initial conditions of the assembled satellite

given the initial conditions. Therefore it is possible to proceed and simulate the system in the space environment. The needed tools, e.g. the control systems, and the simulation will be discussed in the next chapters.

Chapter 3

Position and Attitude Control Systems

In space missions involving multiple satellites, maintaining precise relative position and orientation is pivotal for achieving various objectives such as docking, formation flying, and servicing. To achieve this, it is crucial to design effective position and attitude control systems that can regulate the motion of the satellites.
In this chapter, the position and attitude control systems designed for the previously described contact scenario will be discussed. Two different control strategies have been designed and implemented: the Proportional-Integral-Derivative (PID) controller for attitude control and the Linear Quadratic Regulator (LQR) controller for position control.

The first section of this chapter will provide an overview of the actuation systems used to control the position and attitude of the satellites. This will include a description of the thrusters and reaction wheels (RWs) used to generate the necessary forces and torques for satellite control.
The second section of the chapter will focus on the position control system, which is responsible for controlling the relative position of the satellites. The LQR controller that was used for this purpose will be described, including the development of the state-space model used for control design and the parameters used.
The third section of the chapter will focus on the attitude control system, which is responsible for controlling the orientation of the satellite. The PID controller that was used to control the attitude of our satellites will be described in detail. This will include a discussion of the control law used to generate control signals, the tuned controller gains, and the limitations of the controller.
By detailing the actuation systems and control strategies used, this chapter will provide the necessary foundation for understanding the dynamics and control of the satellites contact system.

3.1 Actuation systems

The actuation systems implemented in this work are thrusters and reaction wheels for position and attitude control respectively. In the following, a detailed description of their characteristics and model will be provided.

3.1.1 Thrusters

Thrusters are a crucial component for every mission that requires a change in position. This could e a necessity for example in station keeping, changing orbit altitude and phasing maneuvers. In this case, an approach maneuver has been studied. To simplify calculations, a 12 thrusters configuration has been considered, as shown in Figure 3.1.

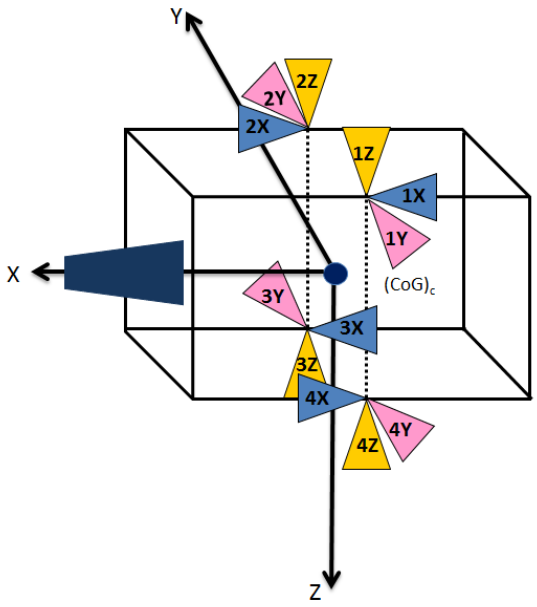

Figure 3.1: 12 Thrusters Configuration.
Adapted from [12].

Force	Thrusters
+X	1X ; 3X
-X	2X ; 4X
+Y	2Y ; 3Y
-Y	1Y ; 4Y
+Z	3Z ; 4Z
-Z	2Z ; 1Z

Table 3.1: Actuation forces with their respective thrusters

This configuration allows to have the thrust always aligned with the spacecraft centre of mass. Therefore, no undesired torques are applied when firing the thrusters. This can be achieved by firing the thrusters as reported in Table 3.1. That is because thrusters can exert only mono-directional actions along their fixed direction, therefore in each control direction a pair of actuators needs to be used.

The chosen thrusters for this application are part of the Standard Micro Propulsion System (MiPS) produced by VACCO. Principal data for these thrusters are also available on the designer's website [13] and are reported in Table 3.2. This is a cold gas propulsion module. Thrusters forces are calculated in the body reference

	VACCO Standard Micro Propulsion System (MiPS)
Nominal Thrust	10 mN
Specific Impulse	40 s
Mass	542 g

Table 3.2: Principal Thrusters Characteristics

frame and have to be converted in LVLH frame for the Hill's equations if the two frames are not aligned.

Thrusters are on/off devices, therefore they can have only two outputs: 0 or U_{max}, where U_{max} is their nominal thrust. To make the model more similar to a real application, a Pulse-Width/Pulse-Frequency (PWPF) modulator has been implemented. This system modulates both the pulse width and the pulse frequency, and gives a quasi linear operation of the thrusters. The control system could require a force that is higher than what the actuation system can provide. For this reason, it has to be modulated. The main element of this modulator is the Schmitt trigger, which is made of a double relay with hysteresis, separated by a dead band. In order to provide a quasi-linear steady-state response, a modulation filter is added. A theoretical block diagram of the described modulator is presented in Figure 3.2.

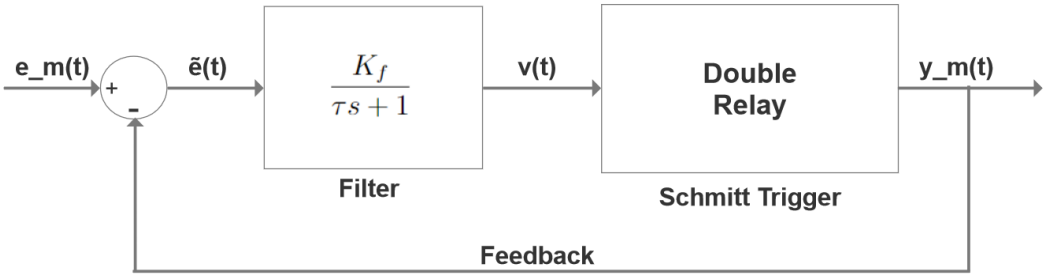

Figure 3.2: Simple diagram of a PWPF modulator

Its input is the signal $\tilde{e} = e_m - y_m$, i.e. the difference between the control signal and the modulator output, and it is represented by a first order system.

The output of the filter is the Schmitt trigger activation signal. The parameters U_{on},U_{off},K_f and τ need to be defined for the correct functioning of the system. These parameters are used to define the following values:

- **Dead band**. It is used because sometimes values can fluctuate rapidly above and below a critical threshold. Creating a dead band as a buffer can prevent the fluctuations from triggering the systems unnecessarily. It can be expressed as:

$$e_{db} = \frac{U_{on}}{K_f} \tag{3.1}$$

- $\mathbf{\Delta t_{on}} = t_{off} - t_{on}$ is the run up time of the thrusters and it is calculated as:

$$\Delta t_{on} = -\tau \ln\left(1 - \frac{U_{on} - U_{off}}{U_{max} K_f}\right) \tag{3.2}$$

The output of the modulator remains zero until the signal exceeds the activation threshold U_{on}. When the threshold is crossed the output becomes U_{max}. This output is held until the filtered variable becomes less than U_{off}. The values of the parameters used in this work are listed in Table 3.3.

Parameter	**Value**
U_{on}	$0.006N$
U_{off}	$0.004N$
K_f	0.75
τ	0.0322

Table 3.3: PWPF modulator parameters

In Figure 3.3 the block diagram used for the Simulink implementation of a single axis PWPF modulator is presented. The transfer function block represent the filter previously shown in Figure 3.2. The Schmitt trigger is represented by the use of the double relay, one positive and one negative. Other two identical schemes have been combined in order to have a 3-axes model.

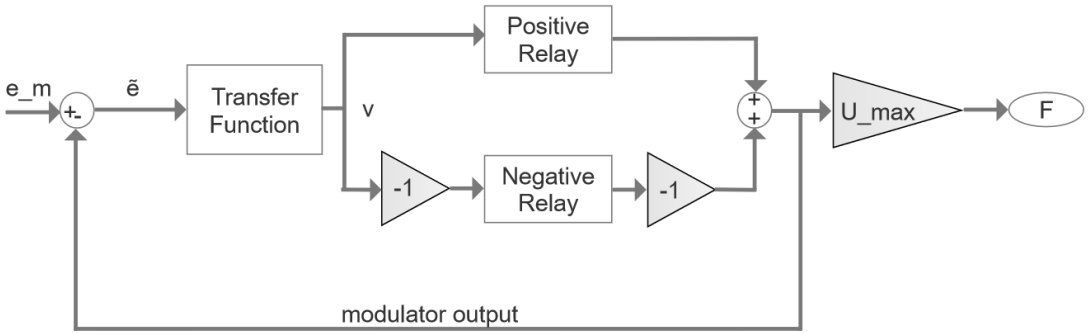

Figure 3.3: Single axis block diagram of the PWPF modulator.

3.1.2 Reaction Wheels

Reaction wheels are common actuation system used for attitude control in small spacecrafts. They are efficient and precise. RWs can exchange angular momentum with the spacecraft using only electrical power that is obtained from the solar panels for the whole lifetime of the satellite. Each wheel is attached to the satellite structure through an electric motor that can be used to accelerate or decelerate the wheel relative to the satellite. This type of actuator applies continuously variable moments to the system. The disadvantage of the reaction wheels use is that they are affected by limitations due to saturation as well as static friction. There are two different types of saturation that a RW can be subject to:

- **Torque Saturation:** the wheel is not able to provide a torque higher than the one for which it has been designed. This is an electrical limitation related to the maximum current that can flow into the motor wires.

- **Momentum Saturation:**when the maximum angular velocity in achieved, the wheel is not able to further accelerate. This is a mechanical limitation, due to preventing bearings damage.

If the wheel reached momentum saturation, it is necessary to desaturate it. In order to do so an external torque needs to be applied using thrusters or magnetorquers. In this application, a pyramid configuration with 4 RWs has been considered. A representation of this configuration is represented in Figure 3.4.

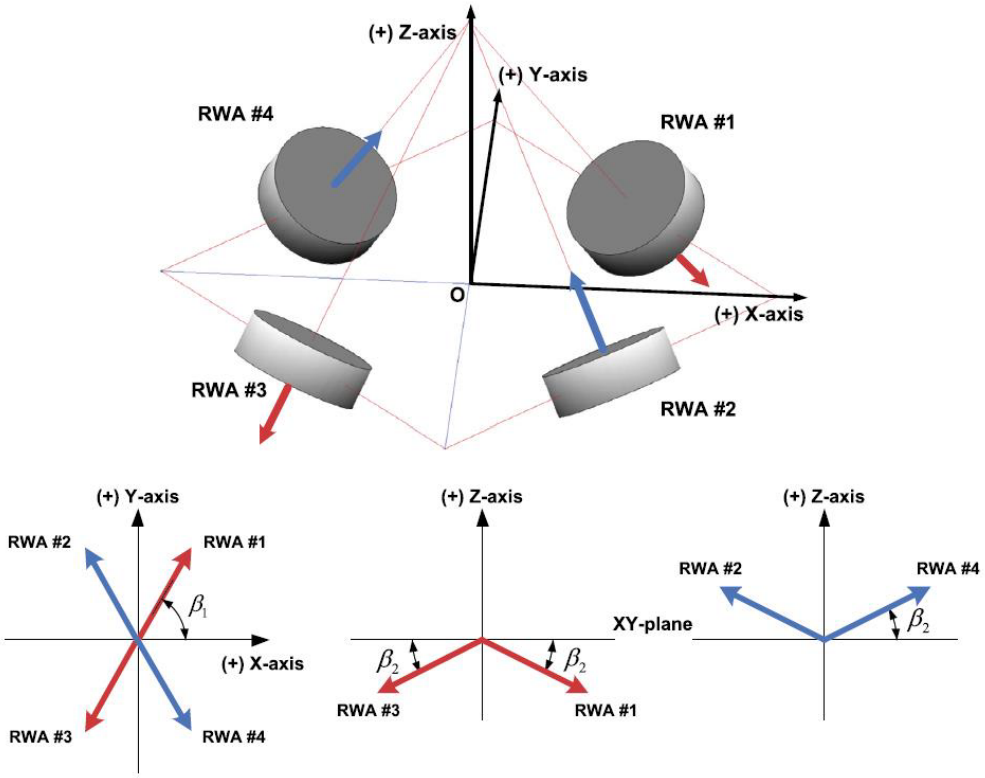

Figure 3.4: Reaction wheels in pyramid configuration. Adapted from [14]

This configuration allows to generate moment along a specific axis while also having redundancy. The main data of the reaction wheels are listed in Table 3.4. The torques given by the actuation systems are in the body reference frame.

RW Data	
RW Maximum Torque	3 $mN \cdot m$
RW Mass	130 g
RW Radius	4.6 cm

Table 3.4: Principal Thrusters Characteristics

The control algorithm gives a control torque in the 3 body axis that has to be transformed to the 4 reaction wheels directions. To do so the following rotation

matrix Z is evaluated:

$$Z = \begin{bmatrix} cos\beta cos\alpha & -cos\beta sin\alpha & cos\beta cos\alpha & cos\beta sin\alpha \\ cos\beta sin\alpha & cos\beta cos\alpha & -cos\beta sin\alpha & -cos\beta cos\alpha \\ sin\beta & sin\beta & sin\beta & sin\beta \end{bmatrix} \tag{3.3}$$

where α and β are mounting angles of the reaction wheels and in this application are set to $\alpha = 0°$ and $\beta = 30°$. Therefore to transform the control signal to the one passed to the 4 RWs the following expression is used:

$$M_{4RW} = Z^{-1} M_c \tag{3.4}$$

where Z^{-1} is a pseudo-inverse matrix. Then, to have the torque on three axes to pass to the attitude dynamics, the following operation is done:

$$M_a = Z M_{4RW} \tag{3.5}$$

To model every reaction wheel a low pass filter, defined using a transfer function, is used along with a saturation block. In Figure 3.5 the block diagram used for the Simulink implementation is presented.

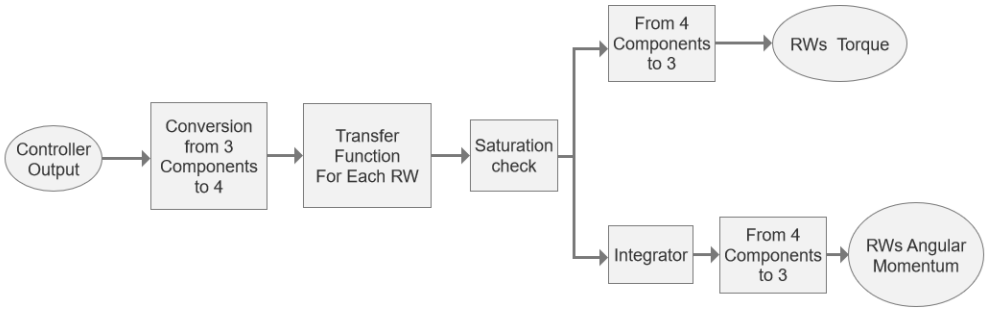

Figure 3.5: Reaction Wheels Block Diagram

For the low pass filter, a transfer function of this form has been used:

$$\frac{1}{\tau_{RW} \cdot s + 1} \tag{3.6}$$

the τ_{RW} parameter of the filter is constant for every reaction wheel and in this application it is set to $\tau_{RW} = 0.1s$. The model receives as an input the output of the attitude control system, and gives as an output the torque provided by the actuation system. As also shown in the block diagram, this output can be integrated to calculate the angular momentum h_{RW}.

3.2 Position Control System

The position control system is used to control the position of the approaching satellite in the LVLH reference frame during the maneuver. An LQR controller has been implemented due to its reliability and robustness This is ideal in space applications where external disturbances are involved. The control law has to be combined with a guidance law that provides the reference trajectory. In this instance, the considered guidance algorithm is the Artificial Potential Field (APF). In this section, the guidance law and the control law will be described.

3.2.1 Artificial Potential Field

The artificial potential field, also described in [10], has been widely used as a guidance algorithm especially in the field of robotics. It allows to also do obstacle avoidance which, while not implemented in this particular application, could be important in the context of avoiding space debris. One of its advantages is that it is intuitive, because the concept derives from the movement of charges in an electrostatic field. It is suitable for on-board planning because the potential can be updated taking into account the motion of the target and the obstacles (if present). APF also solves the kinematic planning of the trajectory by defining the desired speed. Its working principles are listed below:

- an attractive potential is assigned to the target and a repulsive potential is used for the obstacles;
- a paraboloid shape is selected for the attractive force, with a minimum on the target, and an hyperbolic repulsive force for handling the obstacles;
- from the evaluation of the gradient of the total potential, a direction to the minimum potential is evaluated. This vector should be normalized and multiplied by the desired speed;
- Following the evaluated direction, the approaching satellite can reach the target avoiding the obstacles.

The assigned attractive potential has been calculated as follows:

$$U_a(x) = k_a \cdot ||e(x)||^2 \tag{3.7}$$

where k_a is a constant parameter that is set to 1 since no obstacle is present. $e(x)$ is the difference in position between target and chaser:

$$e(x) = \vec{x}_{goal} - \vec{x} \tag{3.8}$$

where $\vec{x}$ is the position of the chaser satellite and $\vec{x}_{goal}$ is the final position of the approach maneuver. To evaluate the attractive force, the following expression has been used:

$$f_a(x) = -\nabla U_a(x) \tag{3.9}$$

The direction of the desired speed is then calculated as:

$$E_U = \frac{f_a(x)}{||\nabla U_a(x)||} \tag{3.10}$$

Therefore the desired speed can be evaluated with the following expression:

$$\dot{x}_d = \dot{x}_{d,max} \cdot E_U \tag{3.11}$$

where $\dot{x}_{d,max}$ is constant and designed by the user. For this application, a value of $\dot{x}_{d,max} = 0.0015$ has been used. This is because one of the goals of this work was to limit the impact velocity between the two satellites, which necessitates a low desired velocity. In Figure 3.6, the block diagram used for the Simulink implementation of the APF is presented.

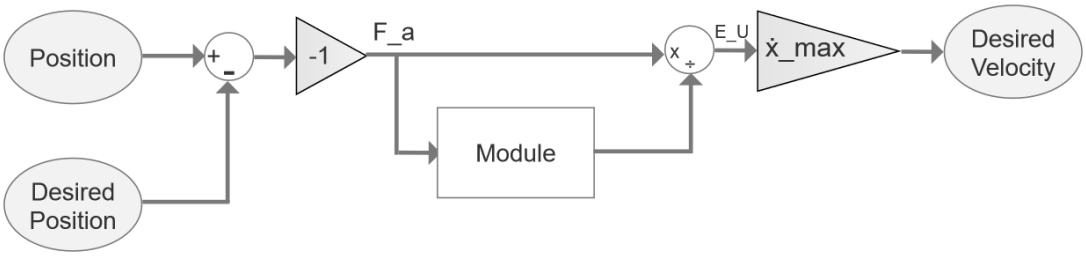

Figure 3.6: APF block diagram

3.2.2 Linear Quadratic Regulator

The linear quadratic regulator is part of the category of feedback controllers. These controllers use the feedback signal from the system to compare it to the desired output. The difference between the two is used to adjust the input to the system. This approach allows to compensate for disturbances or small changes to the system. In order to use an LQR controller, the system dynamics has to be linearized. Therefore the state-space representation is used to describe the dynamics of the system in terms of a set of first-order differential equations. This representation is given as:

$$\begin{aligned} \dot{x}(t) &= Ax(t) + Bu(t) \\ y(t) &= Cx(t) + Du(t) \end{aligned} \tag{3.12}$$

where:

- x is the state vector. In this application the state vector components are the positions and the velocities in all 3 axes, therefore it has 6 components;
- u is the input vector;
- A is the state matrix. Since the LQR controller is used for position control, it is necessary to linearize the position dynamics. Therefore A is obtained from the linearization of the Hill's equation:

$$A = \begin{bmatrix} 0 & 0 & 0 & 1 & 0 & 0 \\ 0 & 0 & 0 & 0 & 1 & 0 \\ 0 & 0 & 0 & 0 & 0 & 1 \\ 3\omega^2 & 0 & 0 & 0 & 2\omega & 0 \\ 0 & 0 & 0 & -2\omega & 0 & 0 \\ 0 & 0 & -\omega^2 & 0 & 0 & 0 \end{bmatrix} \tag{3.13}$$

- B is the input matrix. It also derives from the linearization of the Hill's equations:

$$B = \begin{bmatrix} 0 & 0 & 0 \\ 0 & 0 & 0 \\ 0 & 0 & 0 \\ 1 & 0 & 0 \\ 0 & 1 & 0 \\ 0 & 0 & 1 \end{bmatrix} \tag{3.14}$$

- C is the output matrix;
- D is the transmission matrix and it is set to zero for this application.

The LQR controller is designed based on the state-space representation of the system. The objective of the LQR controller is to find the gain matrix K_{LQR} that generates the optimal control acceleration

$$\vec{\mathbf{a}}_{LQR} = K_{LQR} \cdot \vec{x}_e \tag{3.15}$$

where x_e is the state error. This acceleration minimizes a quadratic cost function of the form:

$$J = \frac{1}{2} \int_0^\infty (x_e^T Q x_e + u^T R u) dt \tag{3.16}$$

where Q and R are the matrices that weigh the state and input variables respectively. These are the matrices to design in order to improve the performance of the

controller. Once matrices Q and R have been defined, the Riccati equation, expressed in equation (3.17), can be solved for P.

$$A^T P + PA - PBR^{-1}B^T P = -Q \tag{3.17}$$

therefore the feedback gain can be computed. as follows:

$$K_{LQR} = -R^{-1}B^T P \tag{3.18}$$

This has been achieved using the MATLAB command $K_{LQR} = lqr(A, B, Q, R)$. The Q and R matrices used in this work are reported in equation (3.19) and equation (3.20).

$$Q = \begin{bmatrix} 10^{-6} & 0 & 0 & 0 & 0 & 0 \\ 0 & 10^{-2} & 0 & 0 & 0 & 0 \\ 0 & 0 & 10^{-3} & 0 & 0 & 0 \\ 0 & 0 & 0 & 10^{-2} & 0 & 0 \\ 0 & 0 & 0 & 0 & 10^{-2} & 0 \\ 0 & 0 & 0 & 0 & 0 & 10^{-2} \end{bmatrix} \tag{3.19}$$

$$R = \begin{bmatrix} 4 \cdot 10^{-3} & 0 & 0 \\ 0 & 40 & 0 \\ 0 & 0 & 4 \end{bmatrix} \tag{3.20}$$

They are both symmetrical and positive definite. The values have been set using a process of trial and error evaluating the response of the system to the different changes in values of these matrices elements.

3.3 Attitude Control System

The attitude control system is designed to regulate the attitude of the approaching spacecraft during the maneuver. Therefore it is a crucial element that allows the magnets to be facing each other at the end of the approach. This is the key factor that consents contact to happen. In this work, a Proportional-Integral-Derivative controller has been used. A quaternion feedback control law is implemented.

3.3.1 Control Law

Quaternions can be easily computed by a modern Attitude Determination and Control System (ADCS), for this reason their use is very common. Therefore a closed loop control based on this information can also be used for on-board control

in autonomous maneuvers. By defining the quaternion vector error $\boldsymbol{q}_e$, the feedback control law can be written as

$$\boldsymbol{M_c} = -\boldsymbol{K}_p\boldsymbol{q}_e - \boldsymbol{K}_d\boldsymbol{\omega}_b \tag{3.21}$$

where:

- $\boldsymbol{M}_c$ is the output of the control algorithm, i.e. the moment that needs to be produced by the reaction wheels;
- $\boldsymbol{\omega}_b$ is the satellite angular velocity;
- $\boldsymbol{K}_p$ and $\boldsymbol{K}_d$ are the gain matrices of the controller. These are the parameters that have to be tuned in order to improve performance;
- $\boldsymbol{q}_e = (q_{1e}, q_{2e}, q_{3e})^T$ is the attitude quaternion vector error which, for the opportune values of $\boldsymbol{K}_p$ and $\boldsymbol{K}_d$, is globally asymptotically stabilizing to the desired attitude $(q_{0,des}, \boldsymbol{q}_{v,des})^T$.

In this control law, there is no integral term, i.e. no $\boldsymbol{K}_I$. Therefore the controller is just a Proportional-Derivative (PD). The quaternion error describes the necessary rotation to align the spacecraft body frame with the target coordinate frame, i.e. LVLH. It can be described as

$$\boldsymbol{q}_e = \boldsymbol{q}_{true} - \boldsymbol{q}_{des} \tag{3.22}$$

where the *true* index stands for the actual quaternion indicating the real attitude of the satellite. This can not be computed as a simple difference. It has to be calculated using the quaternion product, also known as Hamilton product:

$$\boldsymbol{q}_e = \boldsymbol{q}_{des}^{-1} \otimes \boldsymbol{q}_{true} \tag{3.23}$$

The inversion of the quaternion is performed as follows:

$$\boldsymbol{q}_d = \boldsymbol{q}_{des}^{-1} = \frac{\boldsymbol{q}_{des}^*}{||\boldsymbol{q}_{des}||_2} \tag{3.24}$$

where:

- $\boldsymbol{q}_{des}^* = [q_0 - q_1 - q_2 - q_3]^T$ is the conjugate of the desired quaternion;
- $||\boldsymbol{q}_{des}||_2 = (q_0^2 + q_1^2 + q_2^2 + q_3^2)$ is the norm 2 of the desired quaternion.

therefore the quaternion error is expressed by equation (3.25):

$$\boldsymbol{q}_e = \boldsymbol{q}_d \otimes \boldsymbol{q}_{true} = \begin{bmatrix} q_{e0} \\ q_{e1} \\ q_{e2} \\ q_{e3} \end{bmatrix} = \begin{bmatrix} q_{d0} & -q_{d1} & -q_{d2} & -q_{d3} \\ q_{d1} & q_{d0} & -q_{d3} & q_{d2} \\ q_{d2} & q_{d3} & q_{d0} & -q_{d1} \\ q_{d3} & -q_{d2} & q_{d1} & q_{d0} \end{bmatrix} \cdot \begin{bmatrix} q_{true0} \\ q_{true1} \\ q_{true2} \\ q_{true3} \end{bmatrix} \tag{3.25}$$

For the control law the gains $\boldsymbol{K}_p$ and $\boldsymbol{K}_d$ have been calculated as follows:

$$\boldsymbol{K}_p = [\alpha \boldsymbol{I} + \beta \mathbf{1}]^{-1} \tag{3.26}$$

$$\boldsymbol{K}_d = diag(d_1, d_2, d_3) \tag{3.27}$$

where:

- α and β are non-negative scalars;
- $\boldsymbol{I}$ is the 3x3 inertia matrix of the spacecraft;
- $\mathbf{1}$ is the 3x3 identity matrix;
- d_i are positive scalar constants.

In Figure 3.7 the block diagram used for the Simulink implementation of the described controller is presented.

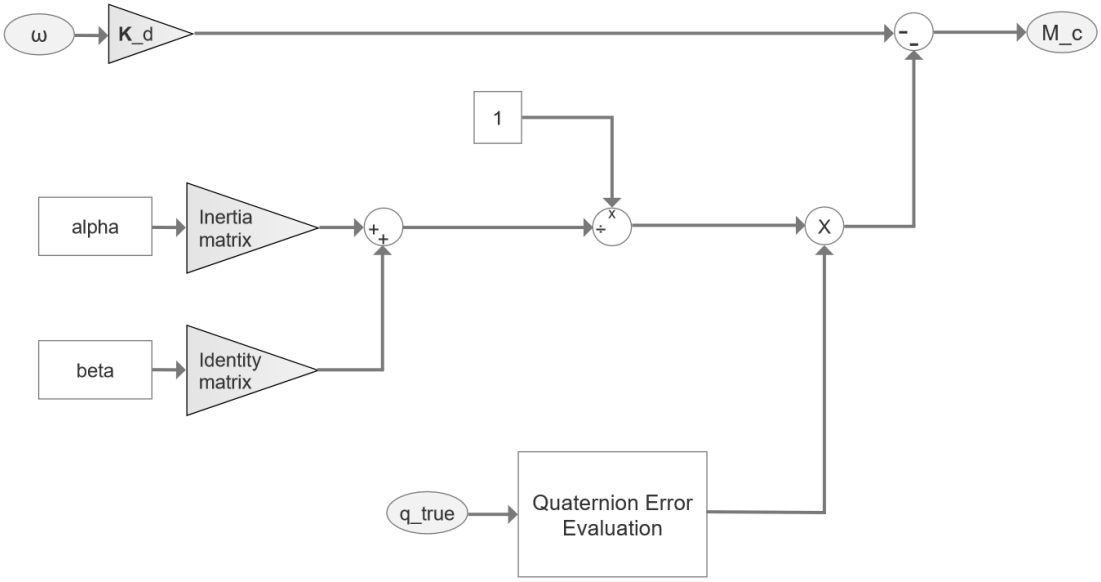

Figure 3.7: Simulink model of the attitude controller

A MATLAB function block has been used to evaluate the quaternion error; its input is the real quaternion of the spacecraft.
To set values for the necessary parameters a process of trial and error has been used. As a guideline for this process, the general rules for tuning a PD controller were used. This set of rules is reported in Table 3.5.

	Rise time	**Overshoot**	**Settling time**	**Steady-state error**	**Stability**
Increasing $\boldsymbol{K}_p$	decrease	increase	small increase	decrease	degrade
Increasing $\boldsymbol{K}_d$	small decrease	decrease	decrease	minor change	improve

Table 3.5: Attitude controller parameters

The reported characteristics are all referred to the transient response of the system. As it can be noted, there is no unique way to tune the controller. This is because changing a parameter to improve one aspect of the system response could lead to the degradation of another one. For this reason, the tuning process needs to be a trade-off. Moreover, the most important aspects of the response to focus on might change depending on the mission goals. Finally, the values of the parameters used to calculate the gains $\boldsymbol{K}_p$ and $\boldsymbol{K}_d$ for the control law are listed in Table 3.6.

Parameter	**Value**
α	0.098
β	0.98
(d_1, d_2, d_3)	$(6.5, 11.7, 13)$

Table 3.6: Attitude controller parameters

Chapter 4

Simulation Results

In this chapter, simulation study is conducted to investigate small spacecraft docking using magnets. The purpose is to provide a comprehensive analysis of the docking maneuver and its various aspects, contributing to the understanding of satellite-to-satellite contact using magnets.
The chapter is divided into three sections, each focusing on a specific aspect of the simulation. First, a detailed overview of the satellite data used in the simulations is provided. This includes information on the physical characteristics of the two satellites, such as their mass, dimensions, magnets properties.
Then the docking maneuver is analyzed, considering ideal conditions and in the presence of external disturbances. The results of both cases are presented, along with a detailed discussion of the implications of the findings.
At last, the final approach of a rendezvous maneuver is considered as test case. This maneuver is added to consider a real case scenario, where one of the two satellites (called the chaser) has to come close to the target satellite in order to begin the docking maneuver. The section presents the results of the approach maneuver in both ideal and disturbed conditions, and discusses the key challenges and opportunities that arise in each case.

4.1 Satellites/Spacecraft Data

Simulation study is conducted considering two 3U CubeSats. Dimensions and characteristics are summarized in Table 4.1, with ϕ diameter of the magnet and h height of the magnet.

Satellite Data	
CubeSat Category	$3U$
Dimensions (l_x, l_y, l_z) $[m]$	(0.1, 0.1, 0.3765)
Mass $[kg]$	4
Magnet Dimension (ϕ, h) $[m]$	$(6.4 \cdot 10^{-2}, 3 \cdot 10^{-2})$

Table 4.1: Characteristics of the two spacecraft.

In the first scenario, satellites are in LEO orbit (height $400\,km$). This altitude is widely used in various applications, e.g. communication and Earth observation, making it a relevant scenario to study. Additionally, LEO orbits are subject to atmospheric drag, which introduces a significant disturbance component. Circular orbit is considered in order to model spacecraft motion using Hill's equations, as discussed in Section 2.2.3. Disturbances acting on the spacecraft in the test cases are:

- **Atmospheric Drag**. Considered to affect only position dynamics. It is compensated with the use of thrusters.
- **J2 Effect**. Affects position dynamics and therefore it has to be compensated using position actuators, i.e.thrusters;
- **Gravity Gradient**. Affects only attitude dynamics, therefore its effect is compensated by the reaction wheels.

The characteristics of the orbit are listed in Table 4.2

Orbit Characteristics	
Reference Altitude	$h = 400\ km$
Orbit Radius	$r = 6778.145 \cdot 10^3\ km$
Gravitational Parameter	$\mu = 3.986 \cdot 10^{14}\ m^3 s^{-2}$
Orbital Tangential Velocity	$V = \sqrt{\frac{\mu}{r}} = 7.6686 \cdot 10^3\ m/s$
Orbital Angular Velocity	$\omega = \sqrt{\frac{\mu}{r^3}} = 0.0011\ rad/s$

Table 4.2: Main Orbit Characteristics.

In Chapter 3, a detailed description of the actuation systems is given.
In Table 4.3 an overview of their characteristics and significant data is reported for clarity purposes.

Actuation Systems Data	
Thrusters Nominal Thrust	10 mN
Thrusters Specific Impulse	40 s
RW Maximum Torque	3 $mN \cdot m$
RW Mass	130 g
RW Radius	4.6 cm

Table 4.3: Main Actuation Systems Characteristics.

In all the maneuvers described in the following sections of this chapter, CubeSats are positioned with the magnets facing each other and with their body reference frame aligned with the LVLH frame. Therefore there is no need for an initial maneuver, e.g. free drift, to align the systems. In order to accurately describe the two maneuvers presented in this chapter, it is important to note that they have different initial conditions. Therefore, the initial conditions for each maneuver will be detailed in their respective sections for clarity.

4.2 Docking maneuver

The docking maneuver is a crucial phase in which contact between the satellites occurs, and precision and reliability are essential to prevent damage. As in the double integrator example presented in section 2.4.2, the initial conditions of the maneuver in terms of attitude and relative position are of utmost importance. It is worth noting that the conditions chosen for the double integrator example are identical to those used in this case study. The main difference is that the presence of the space environment is considered here. Figure 4.1 provides a schematic representation of the initial conditions to facilitate understanding.

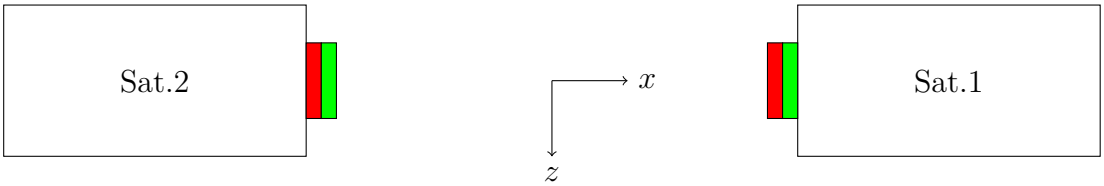

Figure 4.1: Schematic representation of the initial conditions of the docking maneuver.

The origin of the reference frame is positioned in between the two facing satellites. In Table 4.4 are listed the initial condition in terms of position, velocity and angular velocity specific for the maneuver.

	Satellite 1	**Satellite 2**
Starting Position (x_0, y_0, z_0) $[m]$	(0.11, 0, 0)	$(-0.11, 0, 0)$
Starting Velocity (v_{x0}, v_{y0}, v_{z0}) $[m/s]$	(0, 0, 0)	(0, 0, 0)
Starting Angular velocity $(\omega_{x0}, \omega_{y0}, \omega_{z0})$ $[rad/s]$	(0, 0, 0)	(0, 0, 0)

Table 4.4: Initial conditions of the two spacecraft for the docking maneuver.

The starting relative distance between the satellites for the docking maneuver is 22 cm, which has been determined as the maximum distance at which reliable contact can occur. This value was found by performing several simulations with increasing distance between the satellites until contact stopped occurring. If the relative distance between the satellites is greater than this value, contact cannot be achieved using only the magnets due to orbital dynamics. The magnetic force generated by the interaction between the two magnets causes one satellite (Sat.2) to accelerate while the other (Sat.1) decelerates. This causes Sat.2's orbit to rise and Sat.1's orbit to fall, resulting in a change in relative position along the Z_{LVLH} axis.

In the following sections, results for the ideal and real maneuver are presented. It is to be noticed that for this maneuver, no position control was implemented because the satellites already start the simulation in a suitable position for docking. Attitude control has instead been implemented in order to stabilize the system after contact in the real maneuver. The decision to not implement control systems before achieving contact was made to demonstrate that magnets alone can be a reliable means for this type of application, without requiring additional control

measures. Every simulation is conducted in Simulink using a fixed time-step of $0.01s$ and the solver **ode3**.

4.2.1 Docking maneuver in ideal conditions

In the ideal maneuver, disturbances due to the external environment have not been considered. In this section, the results of the ideal simulation are presented. Every aspect will be discussed separately and at the end, a summarizing table will be provided.

The positions of satellite 1 and satellite 2 during the maneuver until contact is achieved, and the position of the assembled system after contact, are represented in Figure 4.2. The red dot represents the contact point and the subscript 'ac' indicates the conditions after contact.

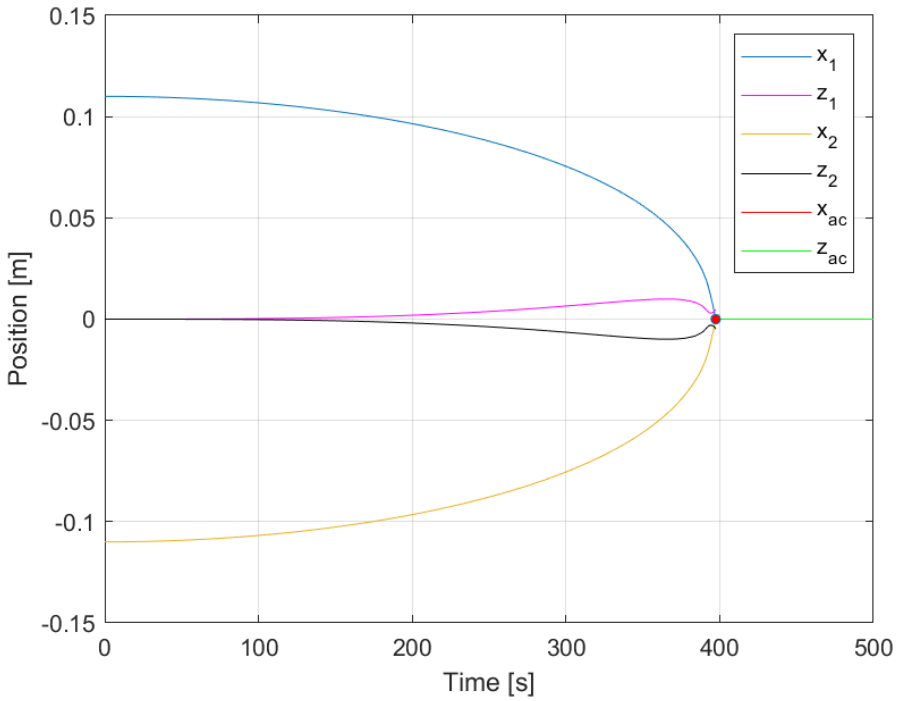

Figure 4.2: Position of the spacecraft before and after contact during ideal docking maneuver.

The figure shows that the magnetic force causes the relative distance between the satellites to decrease until they make contact. The contact occurs when the x component of the position becomes equal for both spacecraft with a margin of 10^{-4} m. However, the z component does not become equal at the moment of contact

due to the coupling of x and z in the Hill's equations and the difference in velocity caused by the magnetic force. The fact that the satellites are not perfectly aligned on the z axis could be avoided by having a physical structure to guide the path to contact, which is common for these scenarios. The contact is achieved after 397.4022 s, and the contact point coordinates are:

$$r_c = (1.4 \cdot 10^{-15},\ 0,\ 0)$$

The centre of mass of the new combined system is the contact point, and the z component is zero because z_1 and z_2 are equal in modulus and opposite in sign. After the contact, no control system is used, but there are no external disturbances therefore the position is stable. The y component of the position is not represented because it is always equal to zero in this case study.

The velocities for the two satellites until contact, and then for the combined system, are shown in Figure 4.3. The subscript 'ac' indicates the conditions after contact.

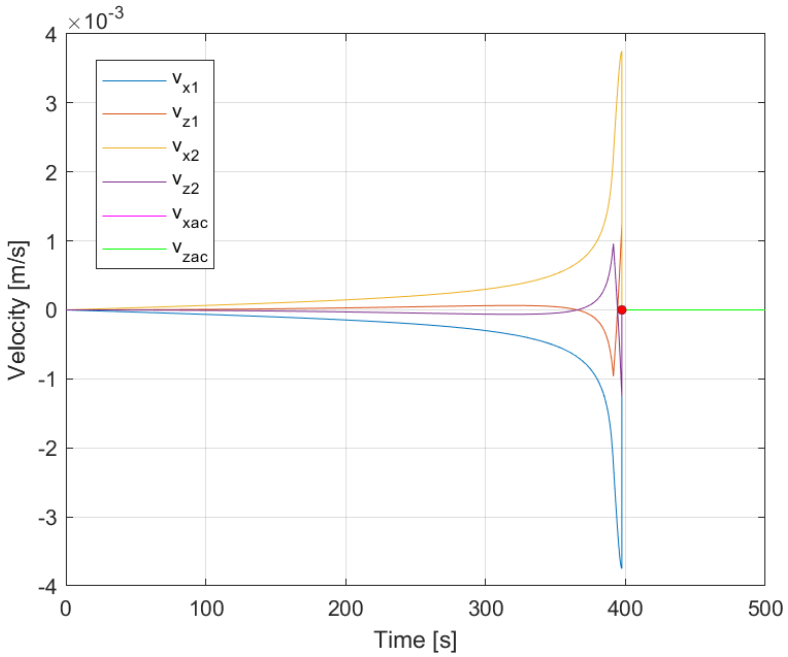

Figure 4.3: Velocity of the spacecraft before and after contact during ideal docking maneuver.

It can be observed that while the spacecraft get closer, their velocity increase. This effect is caused by the magnet interaction, which is intensified the more the magnets are close. At contact, the velocity of each satellite assumes these values:

$$v_{1c} = (-3.8 \cdot 10^{-3},\ 0,\ 1.3 \cdot 10^{-3})\ [m/s]$$

$$v_{2c} = (3.8 \cdot 10^{-3},\ 0,\ -1.3 \cdot 10^{-3})\ [m/s]$$

To calculate the velocity after impact, the conservation of linear momentum is applied as described in Chapter 2 section 2.4. In this ideal case the CubeSats velocities are equal in modulus and opposite in sign, therefore immediately after contact the velocity is zero. Since no disturbances are considered, the velocity remains stable after the contact occurred, as seen in the figure. Also in this case, the y component has been omitted from the graph for better readability since it was always equal to zero. The impact velocity isn't particularly high in this case, but it will be addressed in a later section in order to reduce it. This is because in space is difficult to dissipate heat and energy, therefore it is better to maintain the energy to be dissipated during contact as low as possible.

Figure 4.4 and Figure 4.5 represent the magnetic force applied to Sat.1 and Sat.2, respectively, as a result of the interaction between the magnets.

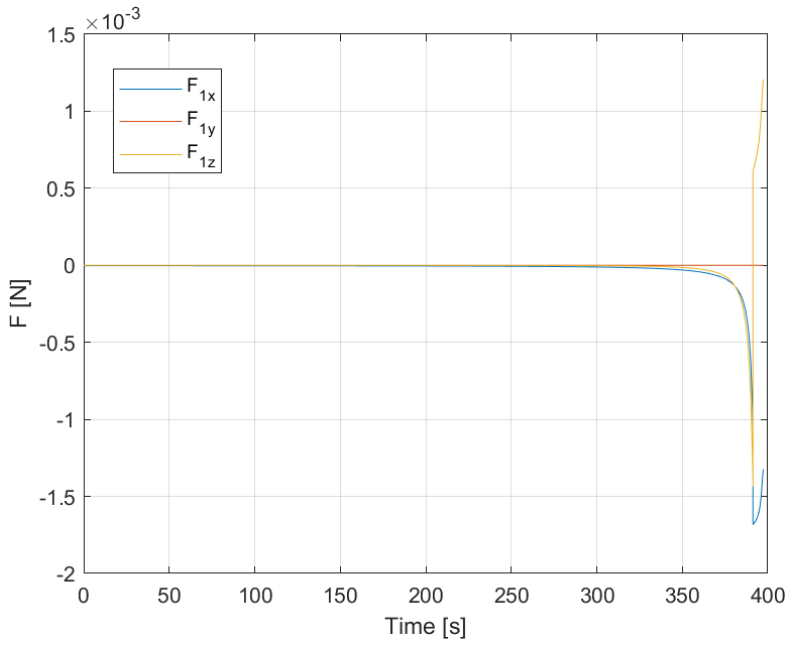

Figure 4.4: Magnetic Force applied on Sat.1 during the ideal docking maneuver.

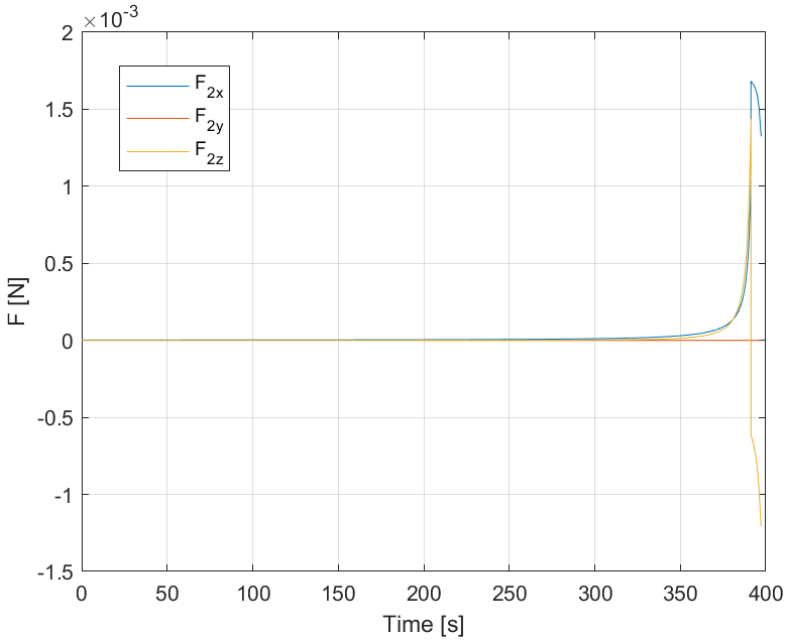

Figure 4.5: Magnetic Force applied on Sat.2 during the ideal docking maneuver.

A notable difference, compared to the double integrator example previously described, is the effect of changes in the z component of the position, which causes the magnetic force to act along this axis as well. It should be noticed that the decrease in F_x towards the end of the maneuver before contact may suggest a reduction in the attraction force, but this is not the case. In fact, the modulus of the total force remains constant and is equal to its maximum value as described in section 2.4.1. This behaviour is due to the fact that the spacecraft are rotating, therefore while F_x is diminishing, F_z is rising and therefore the modulus of F_m remains the same. After the contact is achieved, the magnetic forces become internal forces to the system, therefore they are not considered. The forces at contact for the two CubeSats are:

$$F_{m1_c} = (-0.0013,\, 0,\, 0.0012)\,[N]$$

$$F_{m2_c} = (0.0013,\, 0,\, -0.0012)\,[N]$$

The forces are equal and opposite due to the ideal conditions of the simulation.

In Figure 4.6 and Figure 4.7 the angular velocity profiles of the two satellites are shown. It is manifest that the two spacecraft rotate along the same axis, the same direction, and also the same speed. The angular velocity at contact is equal to:

$$\omega_{1_c} = \omega_{2_c} = (0,\, 0.0238,\, 0)[rad/s]$$

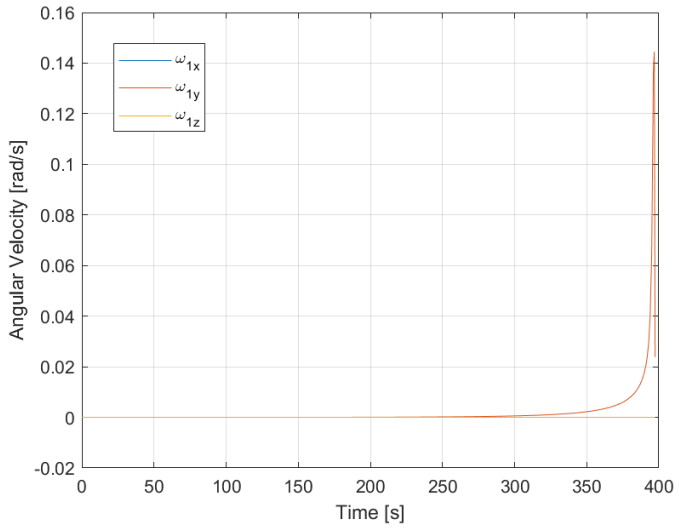

Figure 4.6: Sat.1 angular velocity during the ideal docking maneuver.

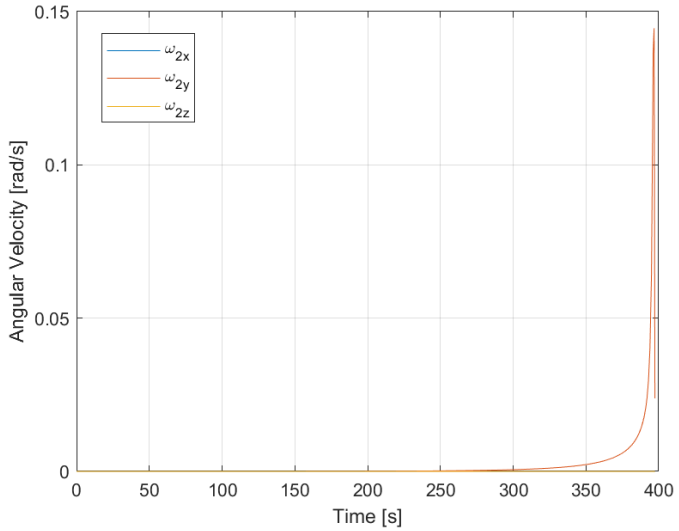

Figure 4.7: Sat.2 angular velocity during the ideal docking maneuver.

By applying the conservation of angular momentum, it can be seen that the angular velocity right after contact is equal to that of a single spacecraft at the contact instant. This implies that without any control actions by the attitude control system, the assembled system would continue to rotate at a constant speed. In this ideal case, no attitude controller was implemented due to the lack of robustness of the PD controller. Therefore, it was decided to tune it directly for the disturbed

maneuver to achieve a better result.

The magnetic torque, which is the cause of the previously described angular velocity, is generated by the misalignment of the two magnets. The magnetic torque profile for Sat.1 and Sat.2 is identical, therefore in Figure 4.8 only the torque applied on Sat.1 is depicted. Its value increases as the distance is reduced, as suggested by the model described in Chapter 2 section 2.4.1. They are equal and applied only in the Y_{LVLH} direction. this is also the reason because the angular velocity profiles are the same for both CubeSats. The torque value at contact is:

$$M_{1c} = M_{2c} = (0,\, 0.0016,\, 0)[N \cdot m]$$

Similarly to the magnetic force, once contact is achieved, the magnetic torques become internal torques, therefore are not considered anymore for calculations.

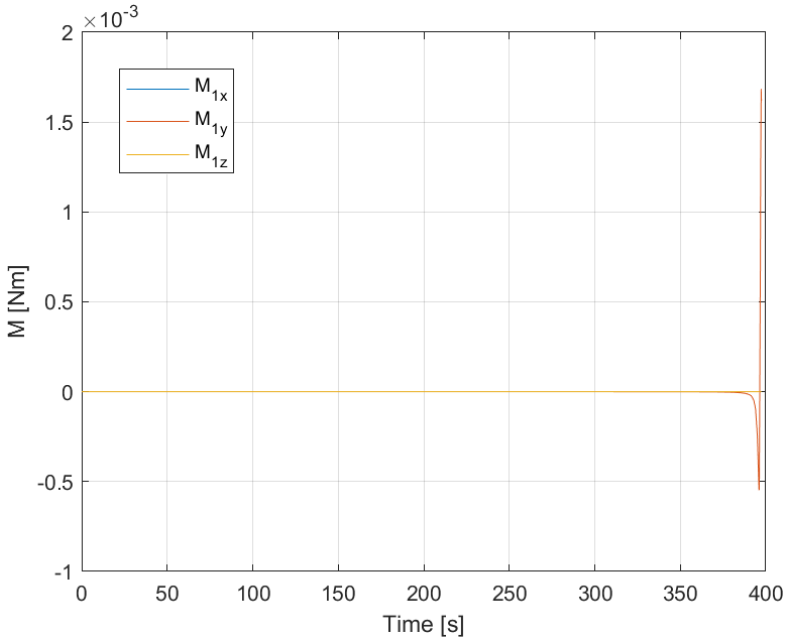

Figure 4.8: Magnetic Force applied on Sat.1 during the ideal docking maneuver.

These torques and angular velocities cause a change in the satellite attitude. This can be represented using quaternions. Since in this case torques M and angular velocities ω are equal for both spacecraft, their attitude change will also be equal. For this reason, only the quaternions of Sat.1 are reported in Figure 4.9.

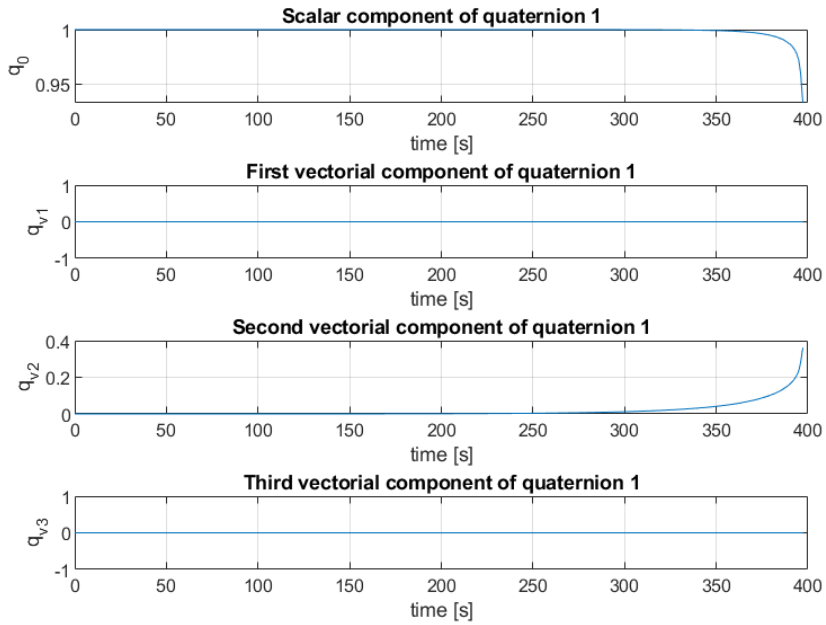

Figure 4.9: Sat.1 quaternion profile during the ideal docking maneuver.

Therefore the attitude at which contact occurs is represented with the quaternion

$$q_c = (0.9326,\ 0,\ 0.3610,\ 0)$$

It is to be noticed that the attitude will be stabilized in the real maneuver by the use of a PD controller managing the reaction wheels. This will bring, after a brief time of assessment, the quaternion back to its desired value:

$$q_{des} = (1,\ 0,\ 0,\ 0)$$

In order to provide more ease of access, Table 4.5 has been included, summarizing the relevant contact values analyzed and aiding in a better understanding of the characteristics of the docking maneuver.

Contact Data for Ideal Docking	
Contact Position	$r_c = (1.4 \cdot 10^{-15},\ 0,\ 0)\ [m]$
Contact Velocity Sat.1	$v_{1c} = (-3.8 \cdot 10^{-3},\ 0,\ 1.3 \cdot 10^{-3})\ [m/s]$
Contact Velocity Sat.2	$v_{2c} = (3.8 \cdot 10^{-3},\ 0,\ -1.3 \cdot 10^{-3})\ [m/s]$
Contact Force Sat.1	$F_{m1_c} = (-0.0013,\ 0,\ 0.0012)\ [N]$
Contact Force Sat.2	$F_{m2_c} = (0.0013,\ 0,\ -0.0012)\ [N]$
Contact Angular Velocity Sat.1	$\omega_{1_c} = (0,\ 0.0238,\ 0)[rad/s]$
Contact Angular Velocity Sat.2	$\omega_{2_c} = (0,\ 0.0238,\ 0)[rad/s]$
Contact Torque Sat.1	$M_{1c} = (0,\ 0.0016,\ 0)[N \cdot m]$
Contact Torque Sat.2	$M_{2c} = (0,\ 0.0016,\ 0)[N \cdot m]$
Contact Attitude	$q_c = (0.9326,\ 0,\ 0.3610,\ 0)$

Table 4.5: Main contact values for the ideal docking maneuver.

4.2.2 Docking maneuver in real conditions

The starting conditions for the maneuver are the same used in the ideal case. The docking maneuver presented in this section also takes into account the external disturbances. The difference with respect to the ideal case will be analyzed. Every aspect of the maneuver will be discussed separately and at the end, a summarizing table will be provided.

In Figure 4.10 the spacecraft position profiles before and after contact are represented. The red dot indicates the contact point for every component. The subscript 'ac' indicates the conditions after contact. Contact is achieved at:

$$t_c = 397.02\,s$$

The main differences from the ideal case can be observed: the y component of the position is no longer zero due to the $J2$ effect, which is the only considered external disturbance affecting this component. Additionally, the atmospheric drag causes an effect of orbital decay, which results in a diminishing value of the z component of Sat.2. In the ideal case, Sat.2 was accelerating due to the magnetic force being its only external force, which caused its orbit to rise.

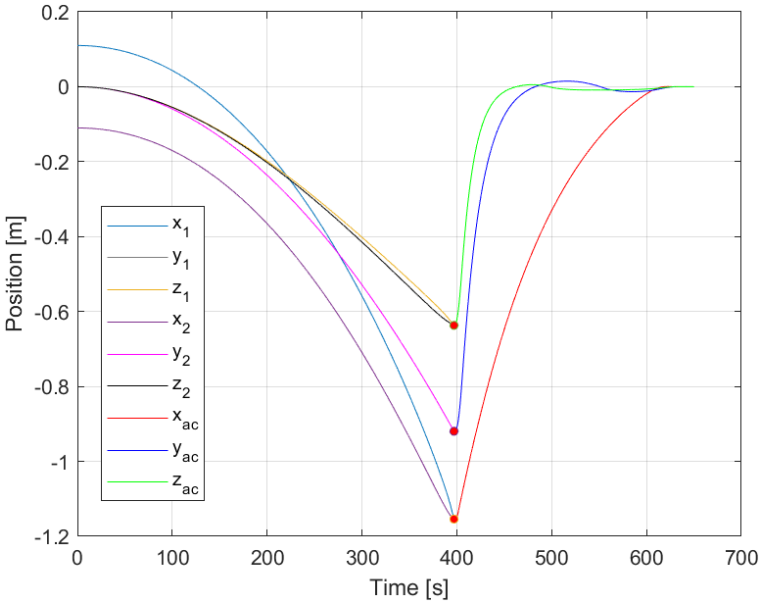

Figure 4.10: Position of every system during all the perturbed docking maneuver.

It can be noticed that the disturbances cause diminishing in every component. therefore the contact point is not (0, 0, 0) as in the ideal case but is:

$$r_c = (-1.1540,\ -0.9197,\ -0.6370)\,[m]$$

After the contact occurred, the position controller is activated to contrast the effect of the disturbances and bring the assembled system back to its desired position of (0,0,0). As it can be seen, the LQR controller described in the Chapter 3 section 3.2, can be used for governing the position of the assembled system. It is here reminded that the thrusters used by the controller are only the ones of Sat.2, therefore only one actuation system is needed.
From there the depiction of the position of the assembled system is shown. The y component for Sat.1 and Sat.2 is the same because is only affected by the $J2$ effect. Therefore their curves overlap.

Figure 4.11 and Figure 4.12 depict, respectively, Sat.1 and Sat.2 velocity profiles.

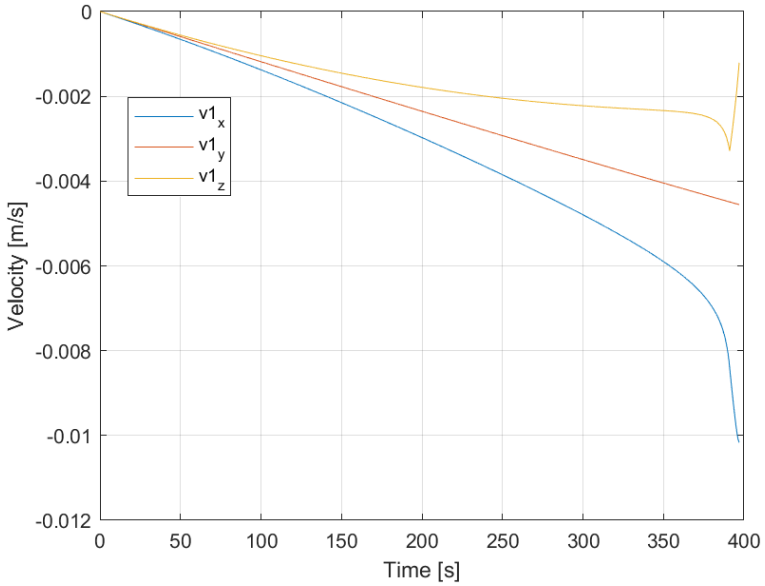

Figure 4.11: Velocity of Sat.1 until contact is reached in the disturbed docking maneuver.

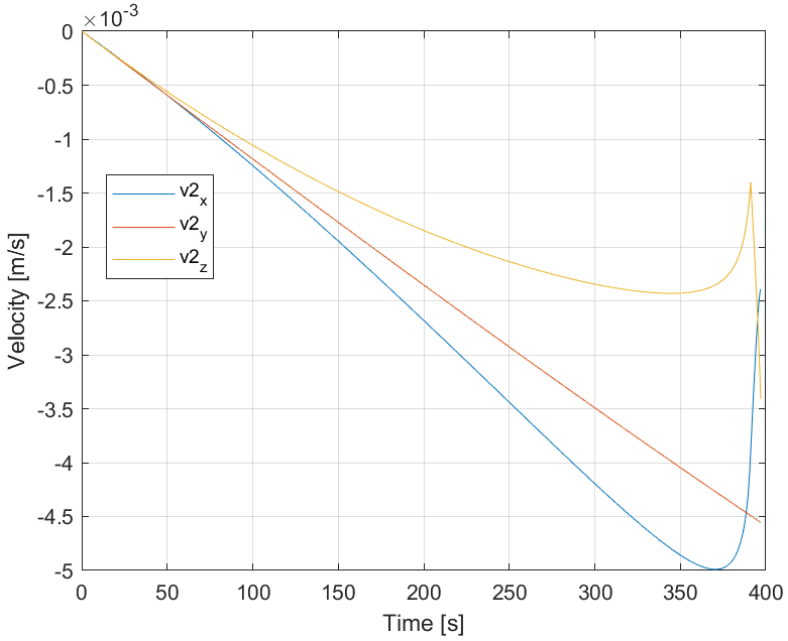

Figure 4.12: Velocity of Sat.2 until contact is reached in the disturbed docking maneuver.

It can be observed that, at first, the satellites are moving predominantly under the

influence of environmental disturbances. When they get closer, the magnetic force gets stronger and as a result has a prevalent effect on the velocity until contact is achieved. The contact velocities for each CubeSat are:

$$v_{c1} = (-1.02 \cdot 10^{-2},\ -4.6 \cdot 10^{-3},\ -1.2 \cdot 10^{-3})\ [m/s]$$

$$v_{c2} = (-2.4 \cdot 10^{-3},\ -4.6 \cdot 10^{-3},\ -3.4 \cdot 10^{-3})\ [m/s]$$

Applying conservation of linear momentum, the velocity immediately after contact is calculated and is equal to:

$$v_{ac} = (-6.3 \cdot 10^{-3},\ -4.6 \cdot 10^{-3},\ -2.3 \cdot 10^{-3})\ [m/s]$$

Which is then modifies by the actuation system in order to control the assembled satellite position.

The magnetic force is calculated as in the ideal maneuver. No particular difference is registered since it is only the spacecraft relative position that is relevant to its model. The magnetic force profiles are represented in Figure 4.13 and Figure 4.14 for Sat.1 and Sat.2, respectively.

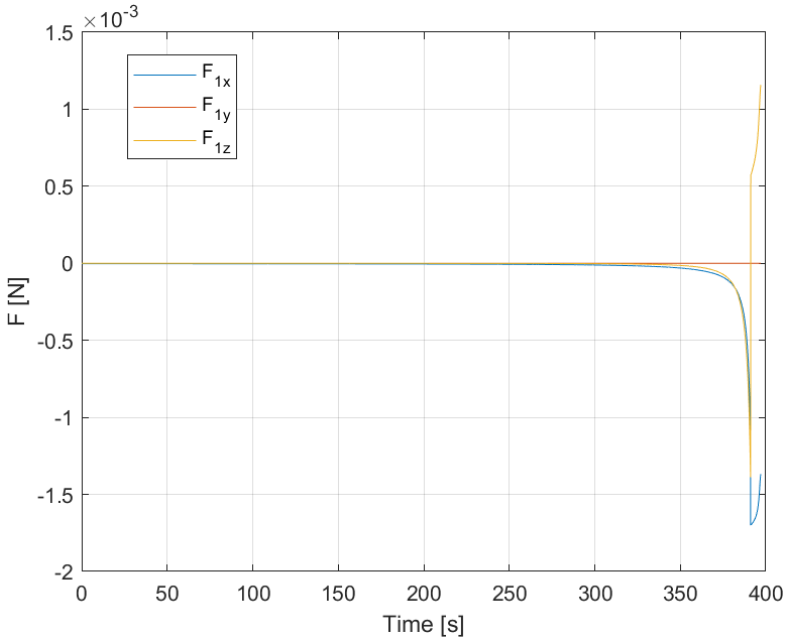

Figure 4.13: Magnetic Force applied on Sat.1 during the disturbed docking maneuver.

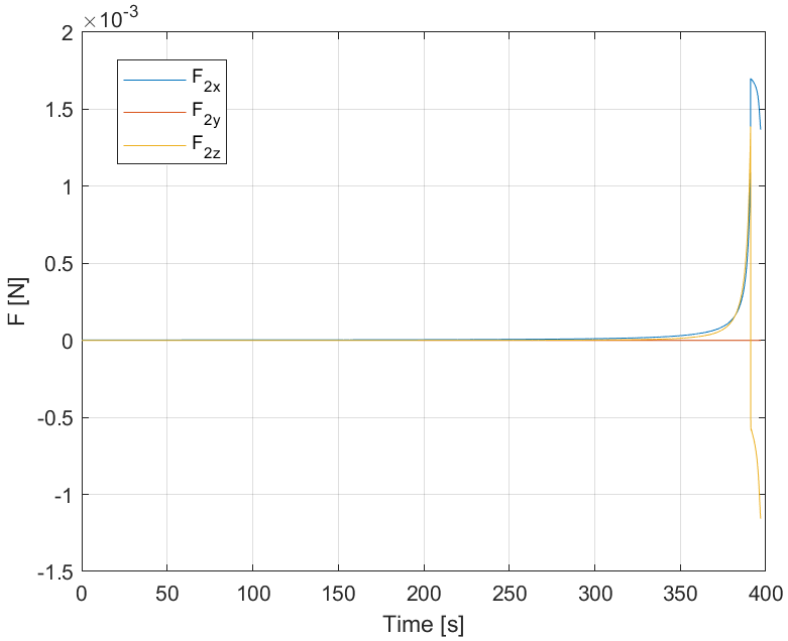

Figure 4.14: Magnetic Force applied on Sat.2 during the disturbed docking maneuver.

The contact values are:

$$F_{m1_c} = (-0.0014,\ 0,\ 0.0012)\,[N]$$

$$F_{m2_c} = (0.0014,\ 0,\ -0.0012)\,[N]$$

After contact, as already discussed, the magnetic force becomes internal and it does not further contribute to calculations.

The angular velocity is caused by the magnetic torque and by the gravity gradient. The first will be described later in this section, the latter has been thoroughly discussed in Chapter 2 Section 2.3.3. Also in this case the angular velocities for the two satellites are equal in modulus and direction. Therefore in Figure 4.15 only the ω value for Sat.1 is shown. Therefore the contact value of angular velocity is:

$$\omega_{1c} = \omega_{2c} = (0,\ 0.0551,\ 0)\,[rad/s]$$

Because the satellites have the same ω, applying the conservation of angular momentum, the angular velocity of the assembled system right after contact is equal to:

$$\omega_{ac} = (0,\ 0.0551,\ 0)[rad/s]$$

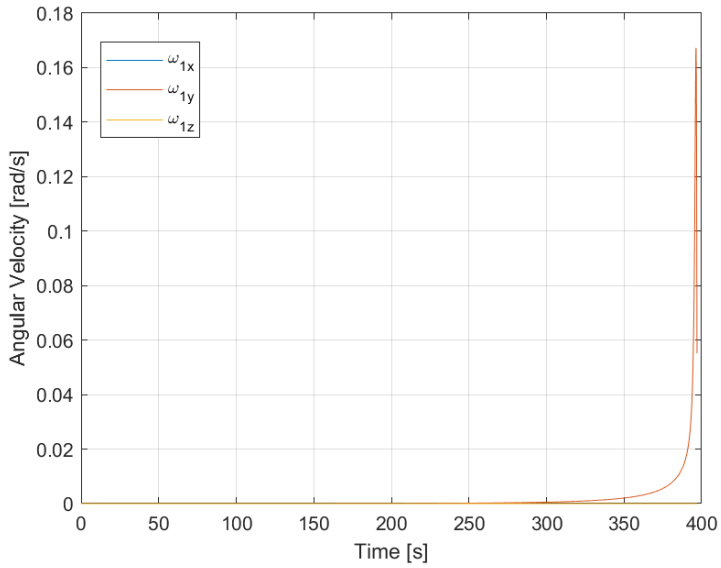

Figure 4.15: Sat.1 angular velocity during the disturbed docking maneuver.

Therefore no change occurs. After the contact is achieved, the attitude control system described in section 3.3 controls the reaction wheels in order to stabilize the system that otherwise would have continued to rotate. The angular velocity profile for the assembled spacecraft is depicted in Figure 4.16.

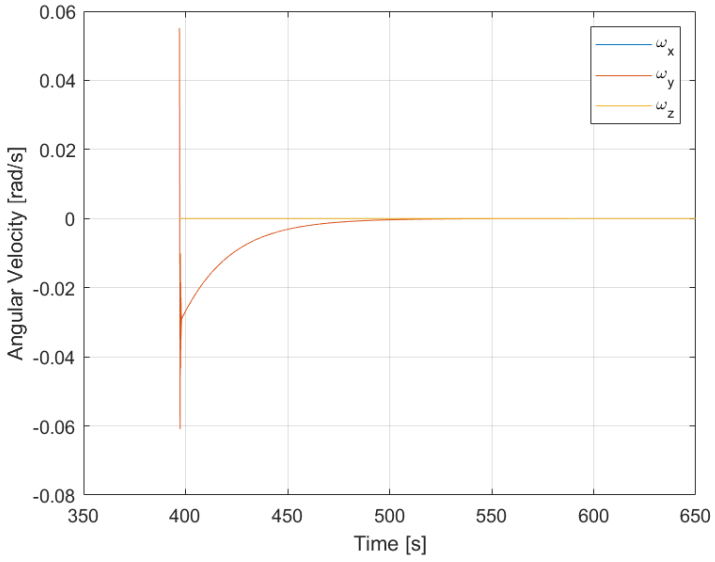

Figure 4.16: Assembled system angular velocity during the perturbed docking maneuver.

It can be seen that, after a brief assessment phase, the PD controller is able to slow down the rotation of the spacecraft and bring it to a stop. It is important to mention that only the actuation system of Sat.2 was used.

In addition to this angular velocity, there is a corresponding change in the spacecraft's attitude. The quaternions profile of Sat.1 is represented in Figure 4.17. The values for Sat.2 are not represented here as they are equal to the ones of Sat.1, therefore they would be redundant. The quaternion value that describes the attitude at the contact instant is:

$$q_c = (0.939,\ 0,\ 0.344,\ 0)$$

Which is similar, but not equal to the one obtained in the ideal case. This is due to the changes induced by the implementation of the environmental disturbances. In figure 4.18 is represented the stabilizing action of the controller that brings the attitude back to its desired value of q_{des}(1,0,0,0).

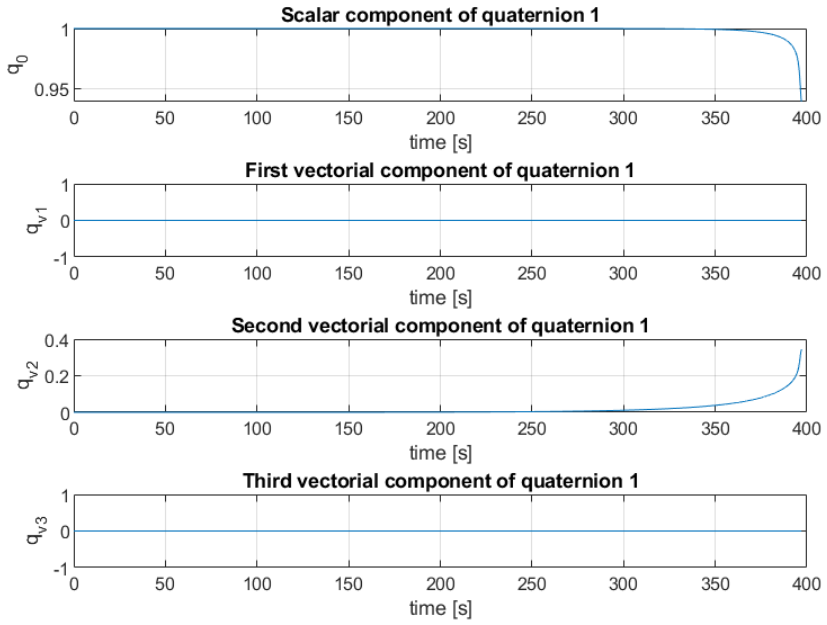

Figure 4.17: Sat.1 attitude during the disturbed docking maneuver.

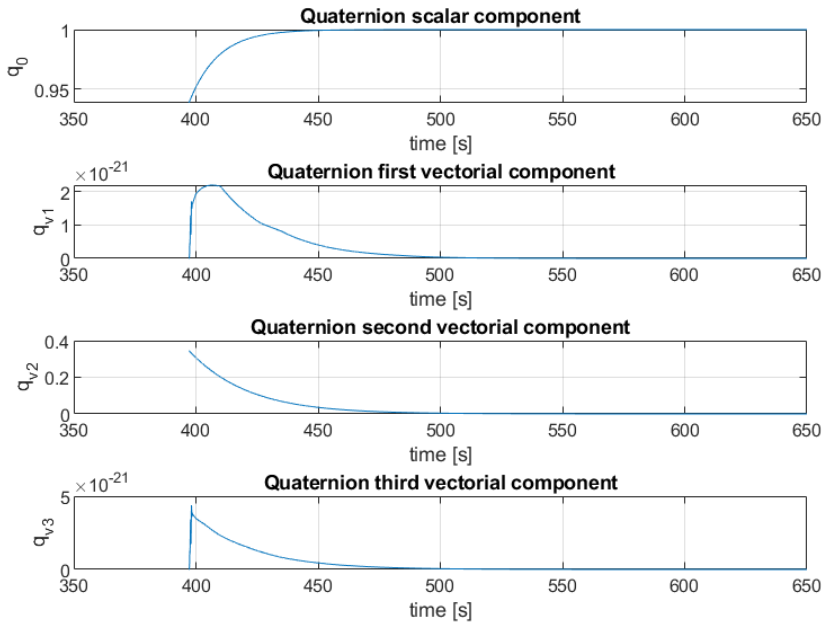

Figure 4.18: Assembled system attitude during the disturbed docking maneuver.

The magnetic torques are calculated as already described for the ideal maneuver. In Figure 4.19 the magnetic force applied on Sat.1 is represented. In this case, similarly to the angular velocity and the attitude, the values for Sat.1 and Sat.2 are equal, therefore only one figure is shown. The contact value for the magnetic torque is:

$$M_{c1} = M_{c2} = (0,\, 0.0019,\, 0)\,[N \cdot m]$$

and after contact it becomes an internal torque and is no longer considered. It is to be noticed that in this maneuver, as well as in the ideal one, the rotation of the spacecraft only happens in the orbit plane $X_{LVLH} - Z_{LVLH}$, therefore along the Y_{LVLH} axis.
To summarize the contact characteristics and provide a more comprehensive overview, Table 4.6 lists the main contact values analyzed during the maneuver.

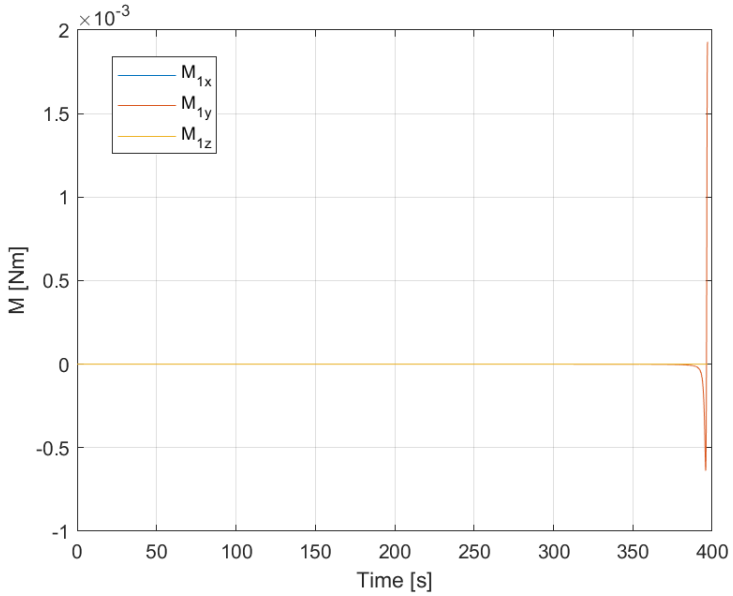

Figure 4.19: Magnetic Torque applied on Sat.1 during the disturbed docking maneuver.

Contact Data for Real Docking	
Time of contact	$397.02\ [s]$
Contact Position	$r_c = (-1.1540,\ -0.9197,\ -0.6370)\ [m]$
Contact Velocity Sat.1	$v_{1c} = (-1.02 \cdot 10^{-2},\ -4.6 \cdot 10^{-3},\ -1.2 \cdot 10^{-3})\ [m/s]$
Contact Velocity Sat.2	$v_{2c} = (-2.4 \cdot 10^{-3},\ -4.6 \cdot 10^{-3},\ -3.4 \cdot 10^{-3})\ [m/s]$
Contact Force Sat.1	$F_{m1_c} = (-0.0014,\ 0,\ 0.0012)\ [N]$
Contact Force Sat.2	$F_{m2_c} = (0.0014,\ 0,\ -0.0012)\ [N]$
Contact Angular Velocity Sat.1	$\omega_{1_c} = (0,\ 0.0551,\ 0)[rad/s]$
Contact Angular Velocity Sat.2	$\omega_{2_c} = (0,\ 0.0551,\ 0)[rad/s]$
Contact Torque Sat.1	$M_{1c} = (0,\ 0.0019,\ 0)[N \cdot m]$
Contact Torque Sat.2	$M_{2c} = (0,\ 0.0019,\ 0)[N \cdot m]$
Contact Attitude	$q_c = (0.939,\ 0,\ 0.344,\ 0)$

Table 4.6: Main contact values for the real docking maneuver.

4.3 Final Approach and Docking

After the docking maneuver has been analyzed, a final approach maneuver has been added to simulate a more realistic scenario. The initial conditions of both satellites, in terms of position, velocity and angular velocity are listed in Table 4.7.

	Sat. 1	**Sat. 2**
Starting Position (x_0, y_0, z_0) $[m]$	(0.093, 0, 0)	$(-200, 0, 0)$
Starting Velocity (v_{x0}, v_{y0}, v_{z0}) $[m/s]$	(0, 0, 0)	(0, 0, 0)
Starting Angular velocity $(\omega_{x0}, \omega_{y0}, \omega_{z0})$ $[rad/s]$	(0, 0, 0)	(0, 0, 0)

Table 4.7: Initial conditions of the two spacecraft for the docking maneuver.

The initial condition of this maneuver differs from the docking one only for the starting position of the two satellites. Therefore the orbit characteristics are the ones listed in Table 4.2. The two satellites (Sat.1 and Sat.2) are the same. The objective of Sat.2 is to position itself at a point that is approximately halfway between the initial starting position of Sat.1 and the maximum distance at which contact can be achieved, accounting for possible errors caused by the position controller. This is the target position of Sat.2:

$$r_{des} = (0,\ 0,\ 0)$$

Maintaining this position will cause Sat.1 to be attracted by the magnet and therefore contact will be established. After contact is achieved, Sat.2 actuation systems will stabilize attitude and position to their desired value.
Similarly to the previous section, ideal and real maneuvers have been analyzed. They will be presented separately and differences will be highlighted.

4.3.1 Final Approach and Docking maneuver in ideal conditions

In this maneuver, no environmental disturbances are considered. All aspects of the maneuver will be discussed separately and, at the end, a summarizing table containing all relevant data will be provided.

This maneuver is not symmetrical as the previous one. Therefore the position profiles are different. In Figure 4.20 the positions assumed by Sat.1 are presented.

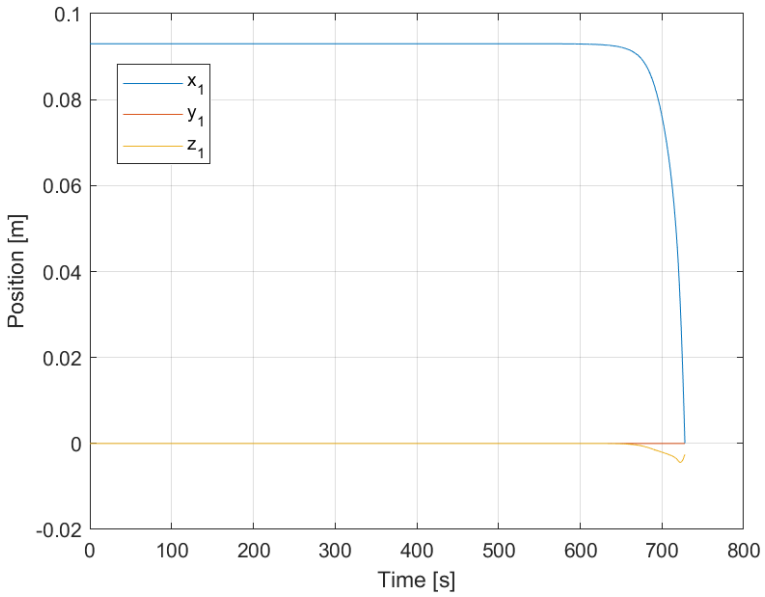

Figure 4.20: Sat.1 position during the ideal approach and docking maneuver.

The CubeSat is undisturbed until Sat.2 arrives close enough to make the interaction between the magnets relevant. From there, the profile position evolves until contact is achieved. In Figure 4.21 the Sat.2 position during the maneuver is depicted.

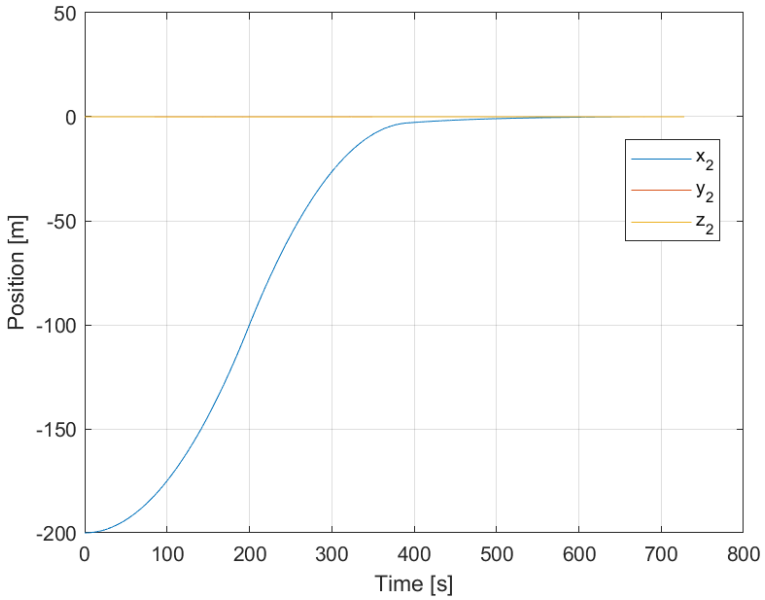

Figure 4.21: Sat.2 position during the ideal approach and docking maneuver.

It can be seen that the LQR controller, which regulates the position, is able to reach

and maintain the desired position until contact occurs. There are no perturbations affecting the y component, therefore it remains equal to zero. The change in the z component is, as previously discussed, due to the coupling of the X_{LVLH} and Z_{LVLH} axes in the Hill's equations. The contact occurs after 728.06 s. The contact point coordinates are:

$$r_c = (-5.62 \cdot 10^{-6},\ 0,\ -0.00127)\,[m]$$

In Figure 4.22 the maintaining of the position of the assembled system after contact is shown. This is operated by the approaching spacecraft thrusters.

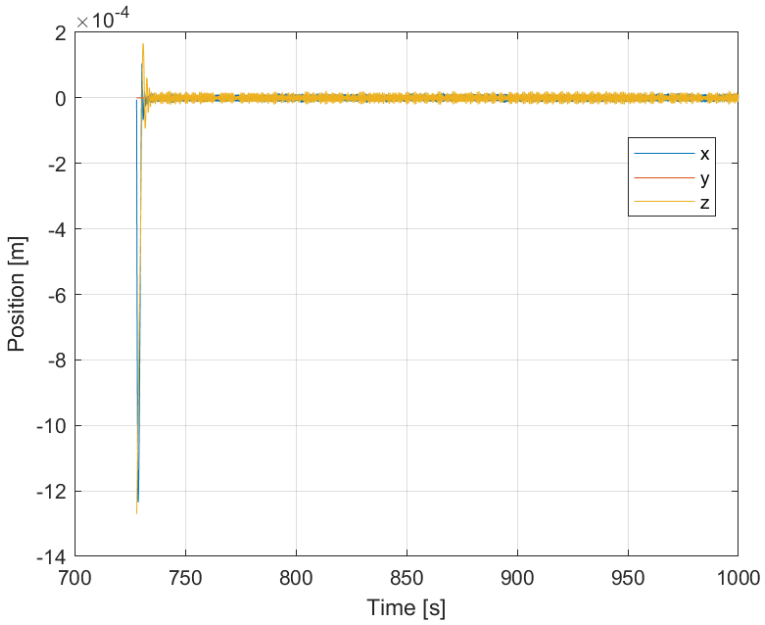

Figure 4.22: Assembled system position during the ideal approach and docking maneuver.

It can be seen that the LQR controller is also suitable for controlling the assembled system with very limited errors.

The velocities of the two spacecraft in this scenario assume very different values. While Sat.1 is undisturbed until the magnetic force begins to be relevant, Sat.2 performs the approach maneuver, therefore the thrusters activate and its velocity changes. The velocities of Sat.1 and Sat.2 are represented in Figure 4.23 and Figure 4.24, respectively.

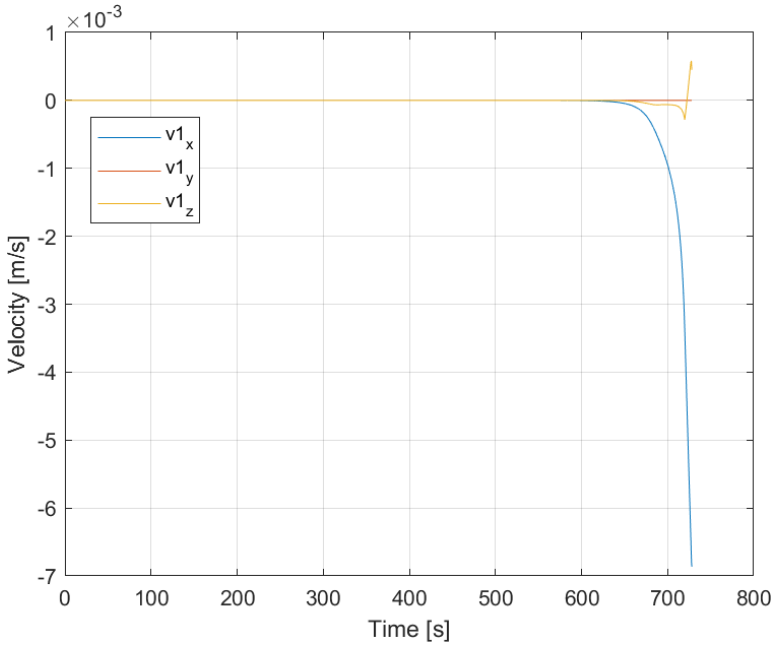

Figure 4.23: Sat.1 velocity during the ideal approach and docking maneuver.

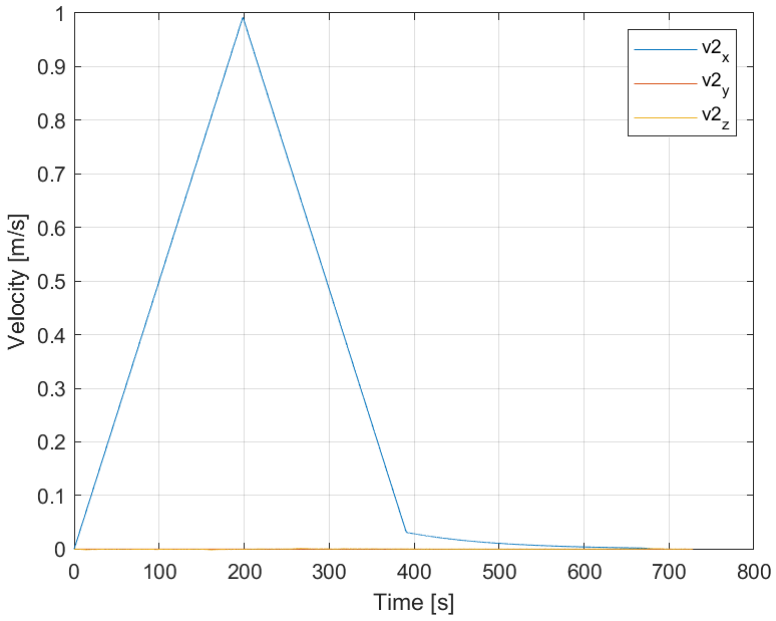

Figure 4.24: Sat.2 velocity during the ideal approach and docking maneuver.

The contact values for this scenario are:

$$v_{1c} = (-6.86 \cdot 10^{-3},\ 0,\ 4.50 \cdot 10^{-4})\ [m/s]$$

$$v_{2c} = (-4.20 \cdot 10^{-5},\ 0,\ 2.49 \cdot 10^{-5})\ [m/s]$$

It is to be noticed that the velocity of the approaching satellite has been significantly reduced compared to the docking maneuver analyzed previously. This is because the satellite is holding its position and therefore it is waiting for Sat.1 to reach contact. This is very beneficial in terms of energy dissipation, which is a crucial factor in the space environment. The velocity of the system right after contact is evaluated applying the conservation of linear momentum, and it is equal to:

$$v_{ac} = (-3.45 \cdot 10^{3},\ 0,\ 2.38 \cdot 10^{-4})\ [m/s]$$

Sat.2 velocity is modified by the LQR controller. It controls the thrusters actuation system that, before contact is achieved, produces the output presented in Figure 4.25.

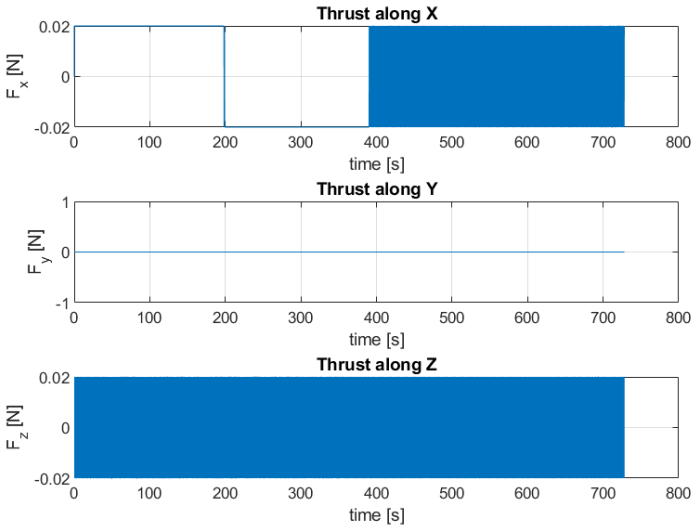

Figure 4.25: Thrusters Force of Sat.2 during the ideal approach and docking maneuver.

The force in the y-direction is zero since there are no disturbances affecting it, and therefore it does not require control. The primary focus of the maneuver is on the x-axis. Initially, a positive thrust is applied to accelerate the spacecraft, followed by a negative thrust to decelerate it. As the target position is approached, both positive and negative contributions are alternately applied to reach and maintain the desired position. The z-component of the force is carefully controlled from the beginning of the maneuver to maintain it as close to zero as possible.

The magnetic force applied on Sat.1 and Sat.2 is represented in Figure 4.26 and Figure 4.27, respectively.

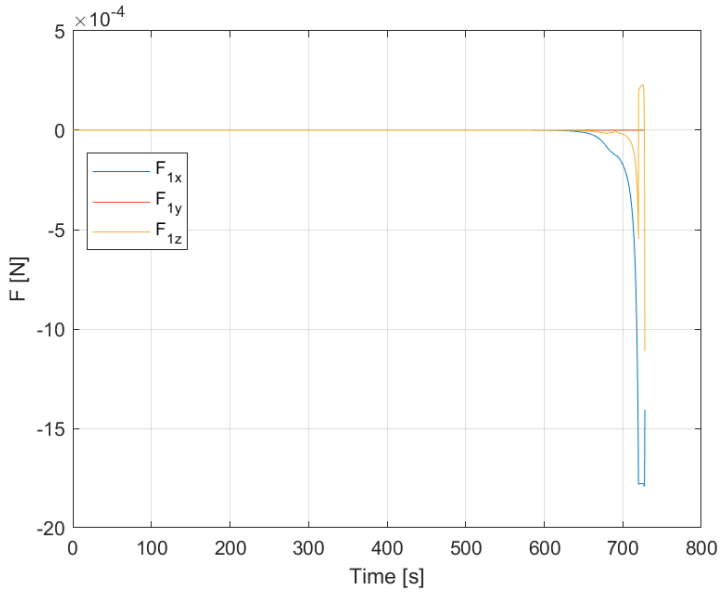

Figure 4.26: Magnetic Force applied on Sat.1. Ideal approach and docking maneuver.

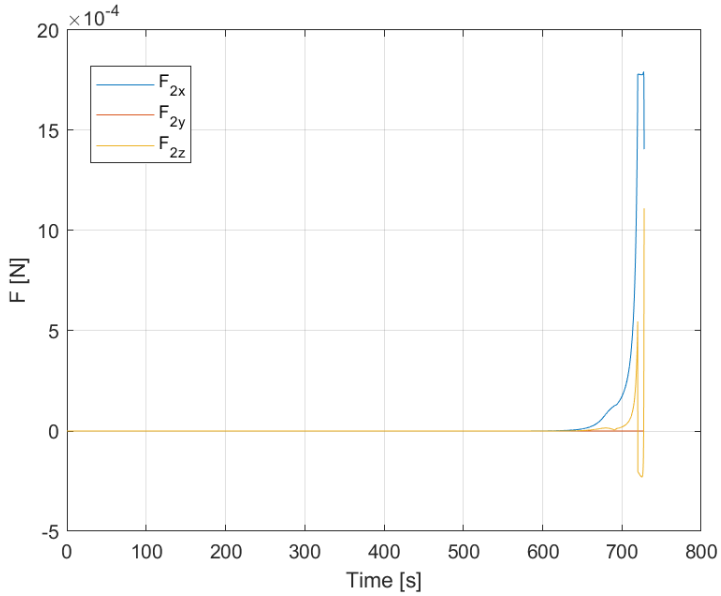

Figure 4.27: Magnetic Force applied on Sat2. Ideal approach and docking maneuver.

It can be seen that the force starts to become relevant only when the satellites become closer together. The contact value is equal to:

$$F_{m1_c} = (-1.406 \cdot 10^{-3},\ 0,\ -1.111 \cdot 10^{-3})\,[N]$$

$$F_{m2_c} = (1.406 \cdot 10^{-3},\ 0,\ 1.111 \cdot 10^{-3})\,[N]$$

The forces are opposite in direction and equal in modulus even in this scenario. This is because they are generated from the same magnets and depend only on the two spacecraft relative position. These forces are external only until contact is achieved. After that, they become internal and are no longer considered.

The spacecraft attitude is represented using quaternions. The attitude until contact is the same for both satellites, therefore only the quaternions of Sat.1 are shown here. They can be observed in Figure 4.28.

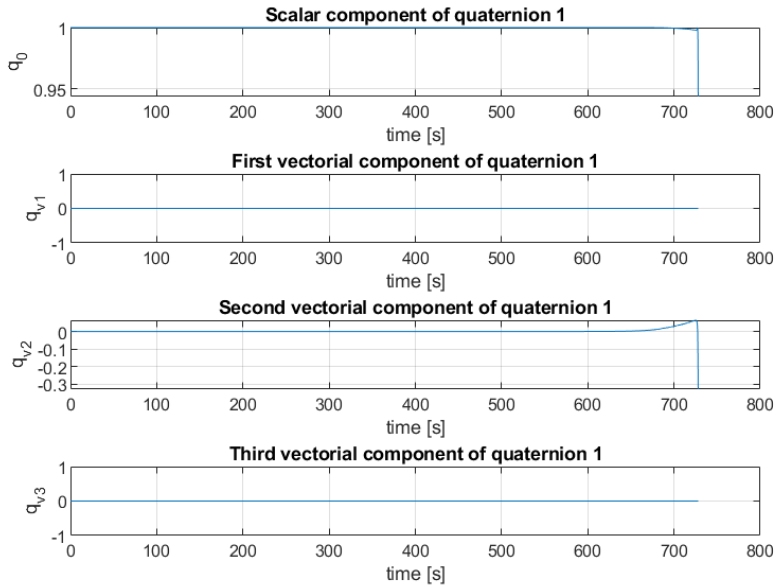

Figure 4.28: Attitude of Sat.1 until contact during the ideal approach and docking maneuver.

The quaternion contact value is:

$$q_c = (0.944,\ 0,\ -0.330,\ 0)$$

Which is also the attitude of the assembled system right after contact. To return to its desired value q_{des} = (1,0,0,0), the attitude control system is used. The attitude

of the combined system after contact is represented by the quaternions profile in Figure 4.29. It can be seen how the actuation system of a single satellite can also stabilize and orient the combined system.

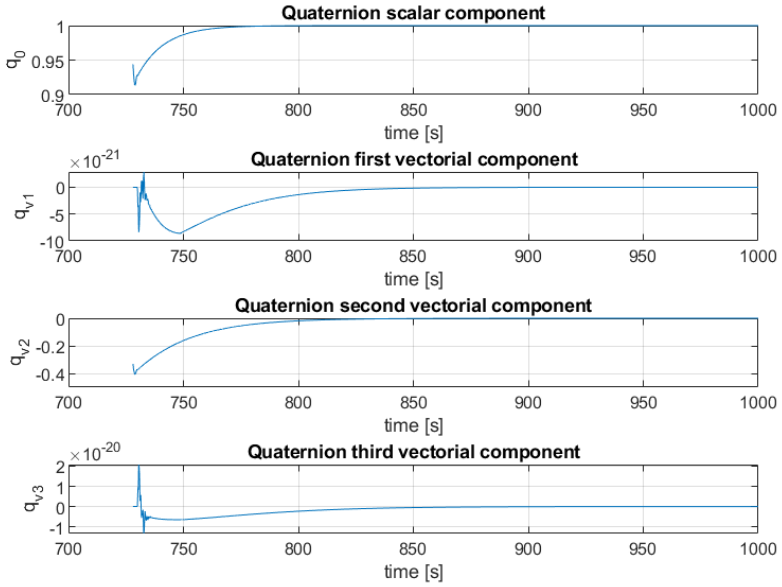

Figure 4.29: Attitude of the assembled system after contact during the ideal approach and docking maneuver.

The angular velocity of the two satellites is equal in this maneuver. For this reason, only the values referred to Sat.1 are presented. Since the maneuver is not perturbed, the angular velocity remains equal to zero during the approach phase and begins to change only when the magnets interaction becomes relevant. Sat.1 angular velocity until contact is represented in Figure 4.30. The contact value for the angular velocity are:

$$\omega_{1c} = \omega_{2c} = \omega_{ac} = (0,\ -0.357,\ 0)\,[rad/s]$$

Applying the conservation of angular momentum, the angular velocity of the combined system right after contact is unchanged. In Figure 4.31 the angular velocities profile after contact is depicted. It can be noticed how, after an initial settling phase, the PD controller is able to stabilize and bring to a stop the combined system rotation. This stabilization is reached, as highlighted before, using only the actuation systems of the approaching satellite.

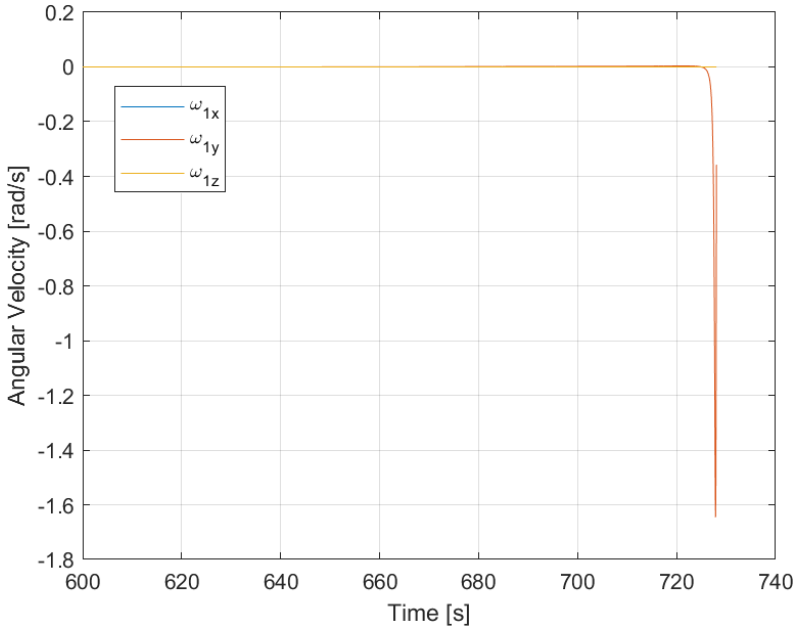

Figure 4.30: Angular velocity of Sat.1 during ideal approach and docking maneuver.

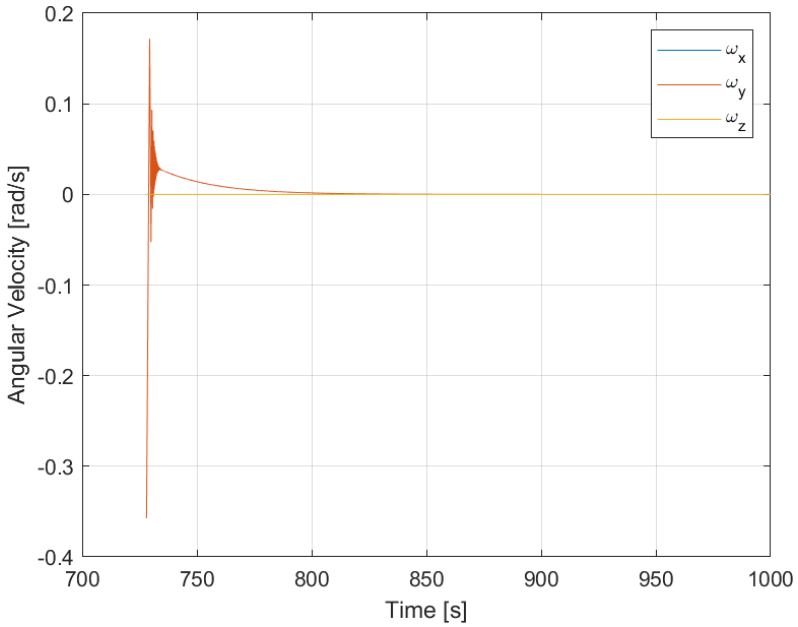

Figure 4.31: Assembled system angular velocity. Ideal approach and docking maneuver.

The magnetic torque that the CubeSats are subjected to, is equal in both direction and modulus. For this reason, only the values for Sat.1 are depicted here. In Figure 4.32 can be found the magnetic torque profile until contact.

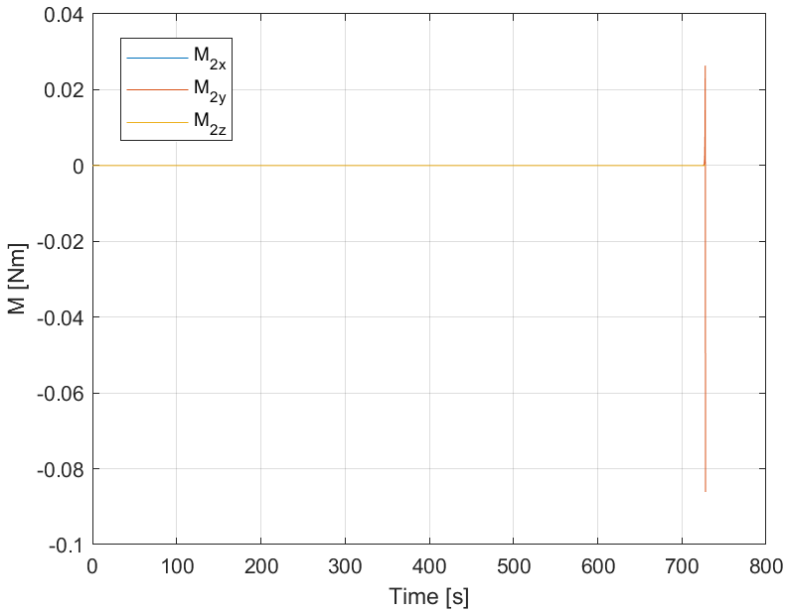

Figure 4.32: Magnetic Torque applied on Sat.1 during the ideal approach and docking maneuver.

It can be observed, similarly to the docking maneuver, that the magnetic torque acts along the orbital plane. Therefore it only has a y component not equal to zero. The more the satellites are close, the more the magnetic torque generated by the magnets interaction is relevant. Its contact value is:

$$M_{1c} = M_{2c} = (0,\ -0.0861,\ 0)\,[N \cdot m]$$

The torque ceases to be considered after the contact is achieved because they become internal to the system.
As a summary for this subsection, all relevant characteristics of the contact of this maneuver are listed in Table 4.8. This aims to provide a comprehensive overview of the maneuver.

Contact Data for Ideal Approach and Docking	
Time of contact	728.06 $[s]$
Contact Position	$r_c = (-5.62 \cdot 10^{-6},\ 0,\ -0.00127)\ [m]$
Contact Velocity Sat.1	$v_{1c} = (-6.86 \cdot 10^{-3},\ 0,\ 4.50 \cdot 10^{-4})\ [m/s]$
Contact Velocity Sat.2	$v_{2c} = (-4.20 \cdot 10^{-5},\ 0,\ 2.49 \cdot 10^{-5})\ [m/s]$
Contact Force Sat.1	$F_{m1_c} = (-1.406 \cdot 10^{-3},\ 0,\ -1.111 \cdot 10^{-3})\ [N]$
Contact Force Sat.2	$F_{m2_c} = (1.406 \cdot 10^{-3},\ 0,\ 1.111 \cdot 10^{-3})\ [N]$
Contact Angular Velocity Sat.1	$\omega_{1_c} = (0,\ -0.357,\ 0)[rad/s]$
Contact Angular Velocity Sat.2	$\omega_{2_c} = (0,\ -0.357,\ 0)[rad/s]$
Contact Torque Sat.1	$M_{1c} = (0,\ -0.0861,\ 0)[N \cdot m]$
Contact Torque Sat.2	$M_{2c} = (0,\ -0.0861,\ 0)[N \cdot m]$
Contact Attitude	$q_c = (0.944,\ 0,\ 0.330,\ 0)$

Table 4.8: Main contact values for the ideal approach and docking maneuver.

4.3.2 Final Approach and Docking maneuver in real conditions

The final approach and docking maneuver presented in this section takes into account external disturbances that affect the spacecraft. In this maneuver, the initial conditions are the same as in the ideal case, but the spacecraft are subject to torques and forces that cause their velocities and angular velocities to deviate from their desired trajectories. In the following, we will analyze the effects of these disturbances on the maneuver and compare them to the ideal case. Sat.1, which is the target spacecraft, is considered undisturbed. This is reasonable because it can be seen as if the satellite is in a station keeping phase. Therefore its state is unperturbed until Sat.2, the approaching satellite, is close enough to cause a relevant magnetic interaction.

The position profiles of the two satellites can be observed in Figure 4.33 and Figure 4.34.

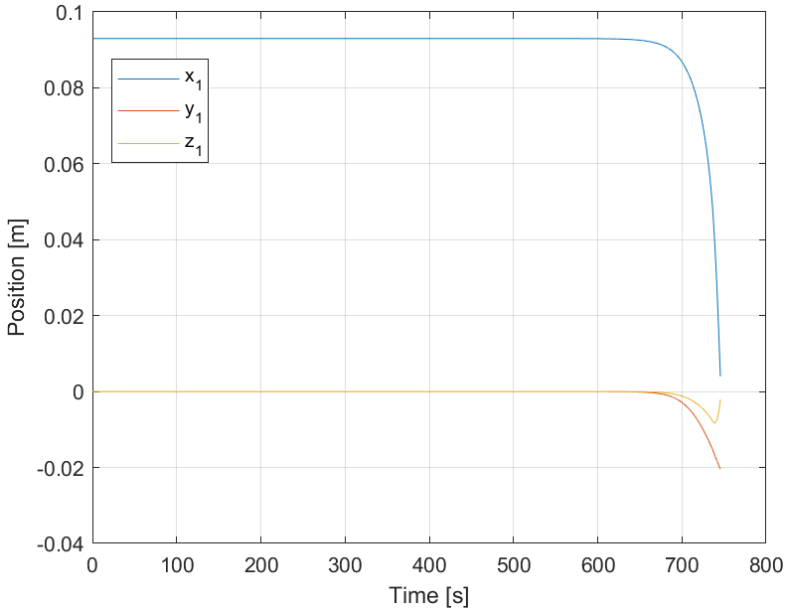

Figure 4.33: Position of Sat.1 during the real approach and docking maneuver.

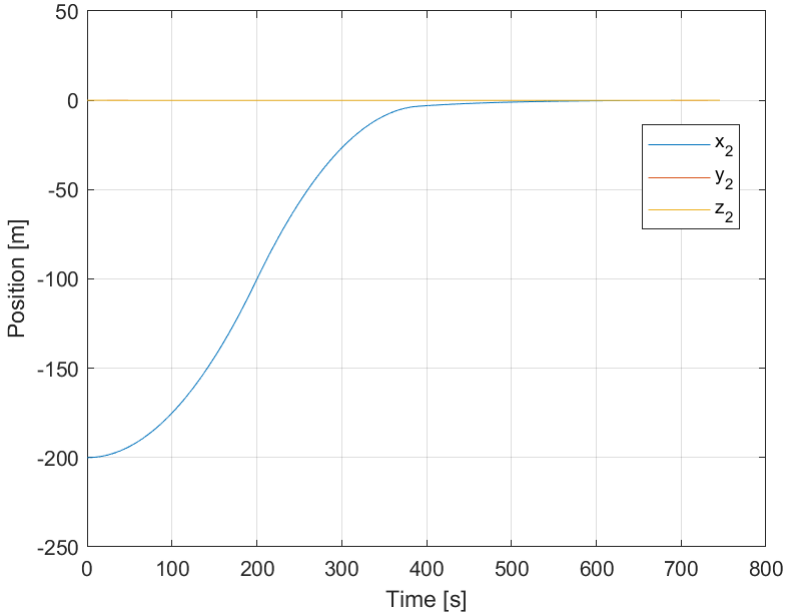

Figure 4.34: Position of Sat.2 during the real approach and docking maneuver.

It is manifest how the LQR controller is able to reach and maintain the desired position even when environmental disturbances are present. Additionally, it can be observed how Sat.1 is not perturbed until Sat.2 is in its close vicinity. Contact is

achieved after 745.67s. Which is slightly more than in the ideal case. This delay in achieving contact can be attributed to the combined effects of the $J2$ effect and atmospheric drag, which result in a slower spacecraft velocity that requires compensation by the actuation system. The contact point coordinates are:

$$r_c = (3.9 \cdot 10^{-3},\ -1.48 \cdot 10^{-2},\ -5.06 \cdot 10^{-3})\,[m]$$

After the contact occurred, the LQR controller, using Sat.2 thrusters, allows the assembled spacecraft to reach and maintain its desired position of r_{des} = (0,0,0). This can be observed in Figure 4.35.

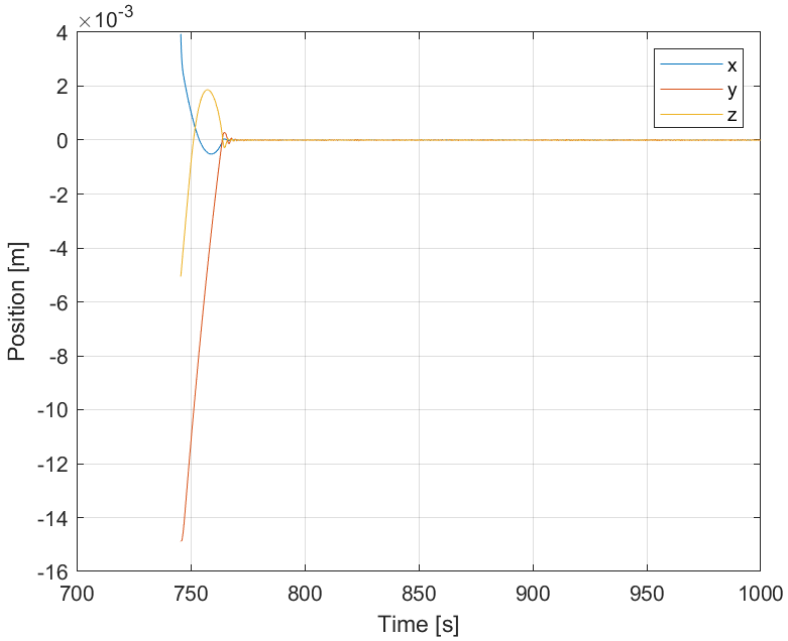

Figure 4.35: Position of the assembled system during the real approach and docking maneuver.

The fact that the controller is able to stably manage the combined system is due to the fact that LQR controllers are generally robust, therefore do not suffer for small changes in the system.

The velocity profile of the systems is very similar to those presented for the ideal maneuver. The velocities of Sat.1 and Sat.2 are depicted in Figure 4.36 and Figure 4.37, respectively. It can be observed that Sat.2 accelerates in order to reach the desired position, then decelerates to approach it slowly enough to maintain it and avoid overshooting.

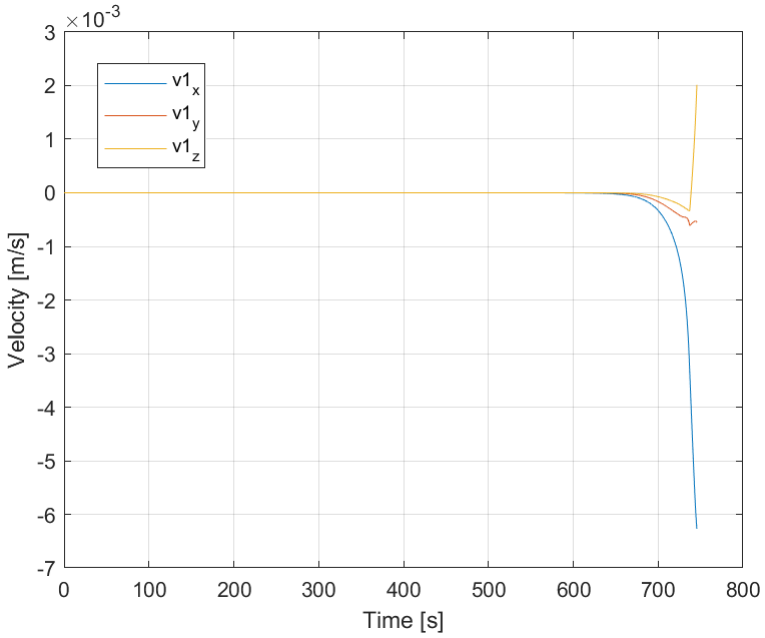

Figure 4.36: Sat.1 velocity during the real approach and docking maneuver.

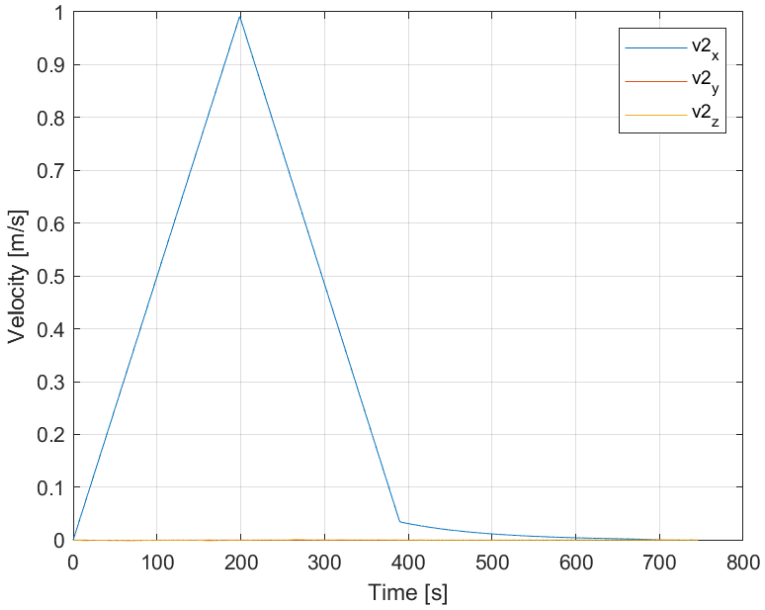

Figure 4.37: Sat.2 velocity during the real approach and docking maneuver.

The velocity changes of Sat.2 are caused by the thrusters. The thrust provided by them, along all 3 axes, is presented in Figure 4.38.

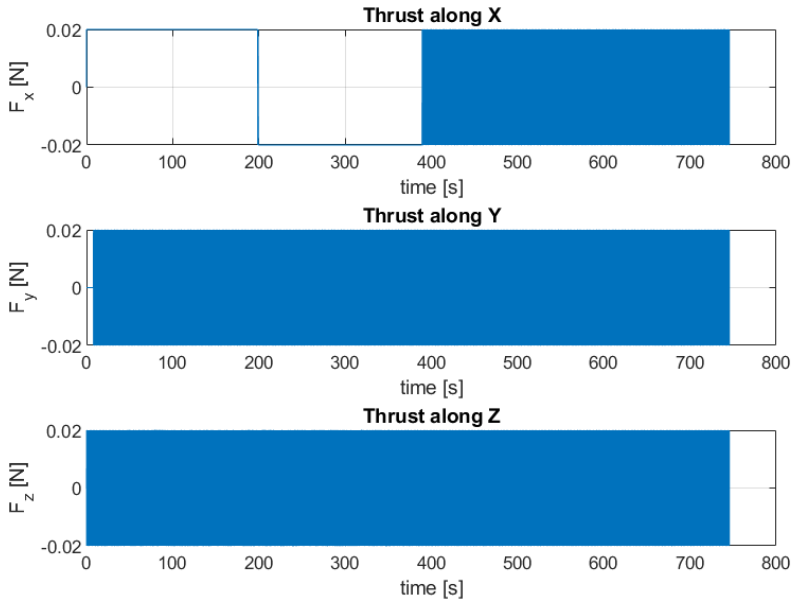

Figure 4.38: Force provided by Sat.2 thrusters during the real approach and docking maneuver.

The main difference with respect to the ideal case is the fact that in this scenario also the y component needs to be controlled.
The contact velocities for both spacecraft are:

$$v_{1c} = (-6.27 \cdot 10^{-3},\ -5.55 \cdot 10^{-4},\ 2.01 \cdot 10^{-3})\,[m/s]$$

$$v_{2c} = (-8.71 \cdot 10^{-5},\ 1.51 \cdot 10^{-4},\ -2.38 \cdot 10^{-5})\,[m/s]$$

Also in this case, the fact that Sat.2 maintains its position allows to reduce the total impact energy that has to be dissipated. The conservation of linear momentum is applied to calculate the resulting velocity of the combined system right after contact, which provides the following value:

$$v_{ac} = (-3.18 \cdot 10^{-3},\ -2.02 \cdot 10^{-4},\ 9.95 \cdot 10^{-4})\,[m/s]$$

The magnetic forces applied on both satellites due to the magnets interaction are represented in Figure 4.39 and Figure 4.40.

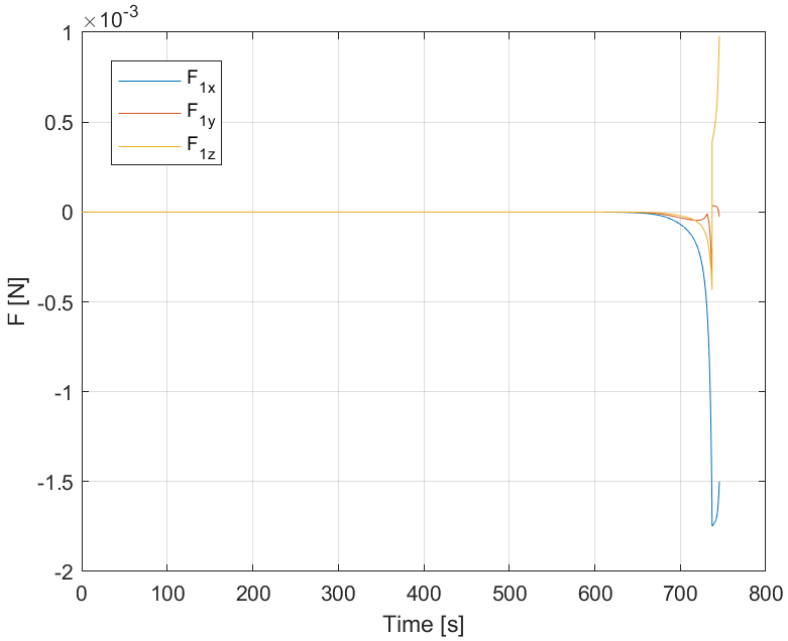

Figure 4.39: Magnetic force applied on Sat.1 during the real approach and docking maneuver.

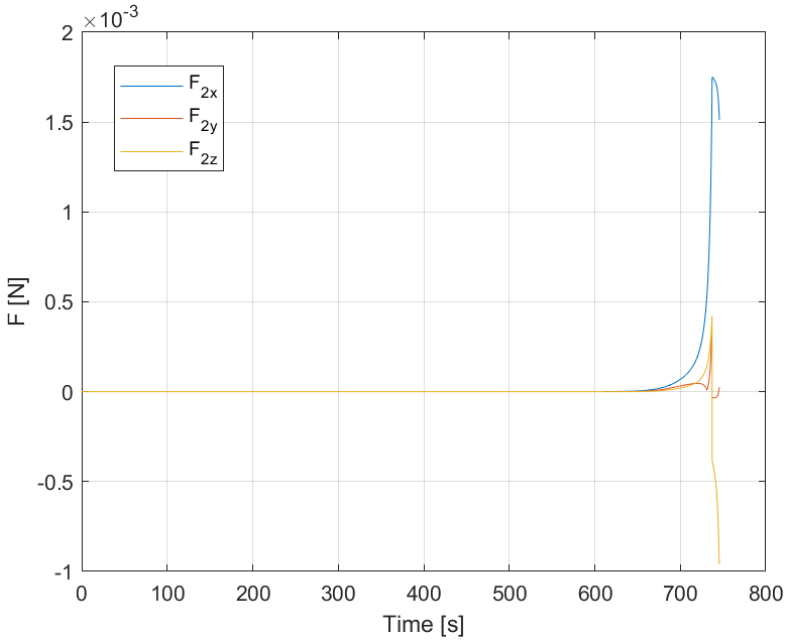

Figure 4.40: Magnetic force applied on Sat.1 during the real approach and docking maneuver.

It can be observed that the forces exerted by the magnets are equal in magnitude but opposite in direction. However, all three force components are not equal to zero, which is attributed to the LQR controller's effort to maintain the position of Sat.2 and compensate for environmental disturbances. Specifically, small misalignments occur along the y-axis, resulting in a force component in that direction.
The contact value of the forces are:

$$F_{m1_c} = (-1.505 \cdot 10^{-3},\ -2.653 \cdot 10^{-5},\ 9.799 \cdot 10^{-4})\,[N]$$

$$F_{m2_c} = (1.512 \cdot 10^{-3},\ 2.557 \cdot 10^{-5},\ -9.602 \cdot 10^{-4})\,[N]$$

After contact, the magnetic force is no longer considered as it becomes internal to the system.

Attitude variations are represented by changes in the CubeSats quaternions. The attitude of both systems is equal until contact. Therefore only the quaternions of Sat.1 are represented in Figure 4.41.

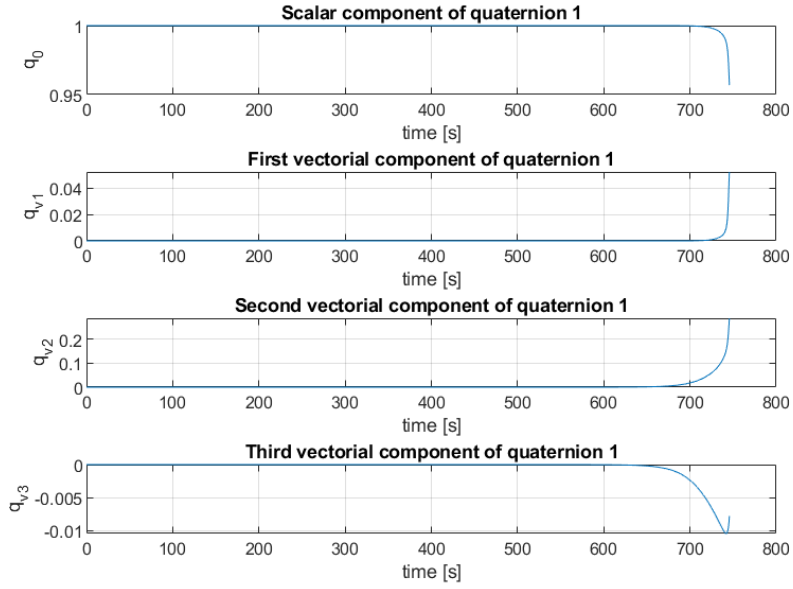

Figure 4.41: Sat.1 attitude during the real approach and docking maneuver.

It can be noticed that the quaternion changes in all its components, differently to the ideal maneuver. This could be expected because forces are now also acting on the y axis. The misalignment causes a torque, which will be described later in this

section, which is the reason for this attitude change.
The contact attitude can be expressed by the following quaternion:

$$q_c = (0.958,\ 0.051,\ 0.279,\ -0.007)$$

Right after contact, Sat.2 attitude control system is activated by the PD controller to bring back and maintain the combined system attitude to its desired value q_{del} = (1,0,0,0). In Figure 4.42 attitude after contact is depicted.

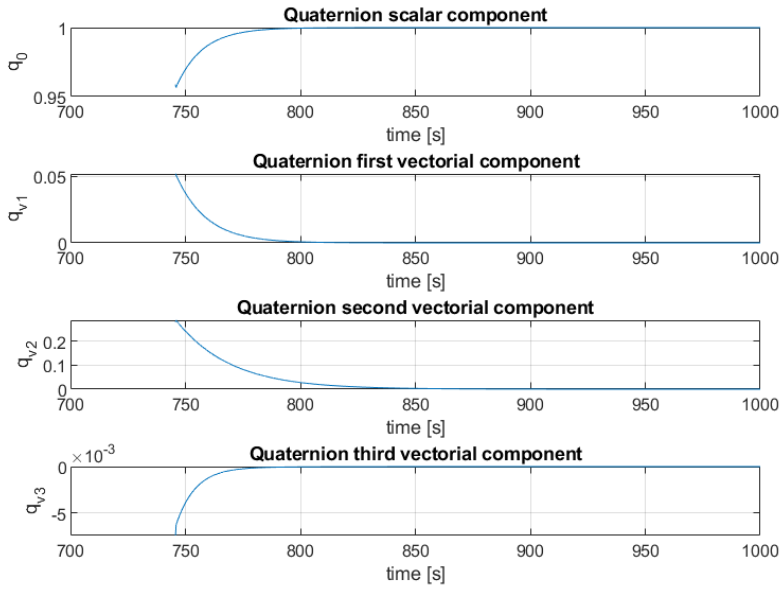

Figure 4.42: Assembled system attitude during the real approach and docking maneuver.

It is manifest that the actuation system is able to manage the assembled spacecraft.

The angular velocity in the ideal maneuver is equal in both magnitude and direction for Sat.1 and Sat.2. This is not the case in this scenario. A minor difference in angular velocity is due to the fact that Sat.1 is considered not under the influence of the external disturbances. Therefore Sat.2 presents a slightly different angular velocity because of the action of the gravity gradient. In Figure 4.43 and Figure 4.44 are depicted the angular velocity profiles until contact is achieved.

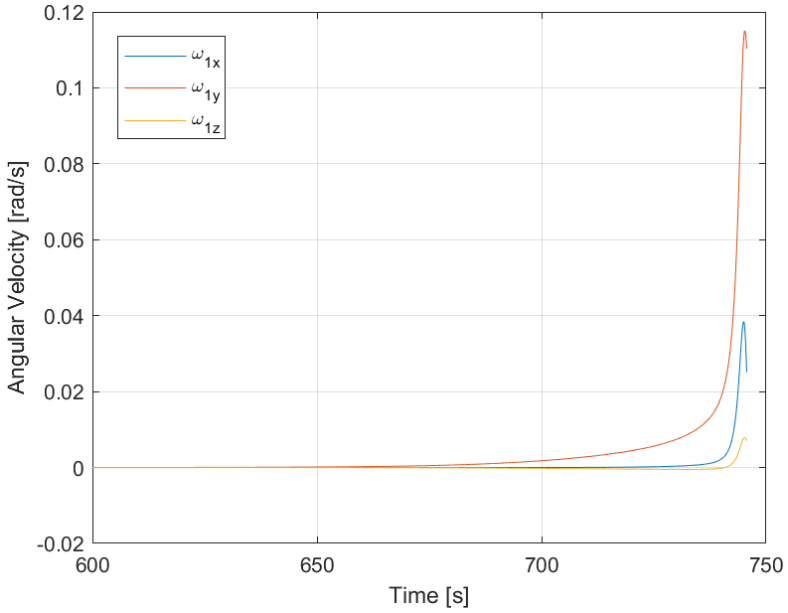

Figure 4.43: Sat.1 angular velocity during the real approach and docking maneuver.

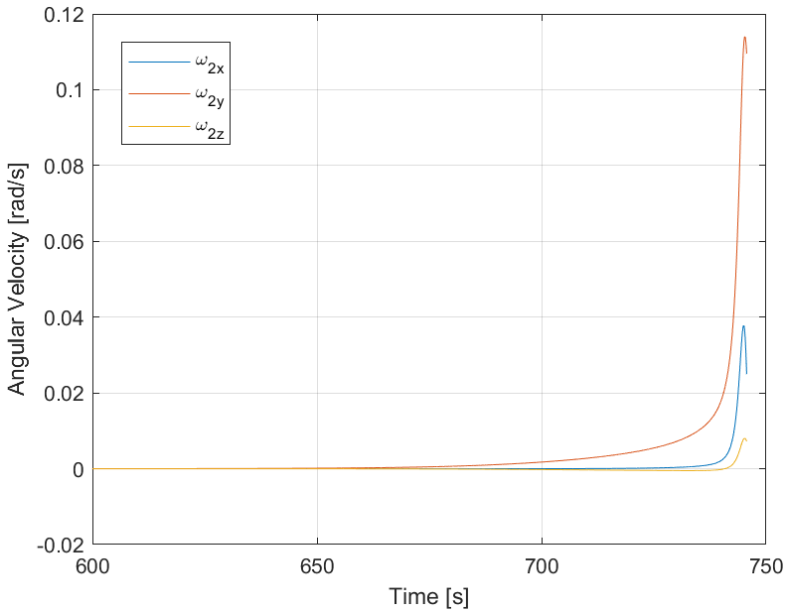

Figure 4.44: Sat.2 angular velocity during the real approach and docking maneuver.

All components become not zero due to the previously discussed causes.

The contact values are:

$$\omega_{1_c} = (2.511 \cdot 10^{-2},\ 0.110,\ 7.097 \cdot 10^{-3})\,[rad/s]$$

$$\omega_{2_c} = (2.492 \cdot 10^{-2},\ 0.109,\ 7.263 \cdot 10^{-3})\,[rad/s]$$

As highlighted by these values, the difference is minor, but still present. Applying the conservation of angular momentum, the angular velocity of the combined system right after contact is evaluated:

$$\omega_{ac} = (2.502 \cdot 10^{-2},\ 0.109,\ 3.590 \cdot 10^{-3})\,[rad/s]$$

After contact is achieved, Sat.2 reaction wheels stabilize the assembled spacecraft and maintain its desired attitude. The actuation system action can be seen in the angular velocity profile of the combined system presented in Figure 4.45.

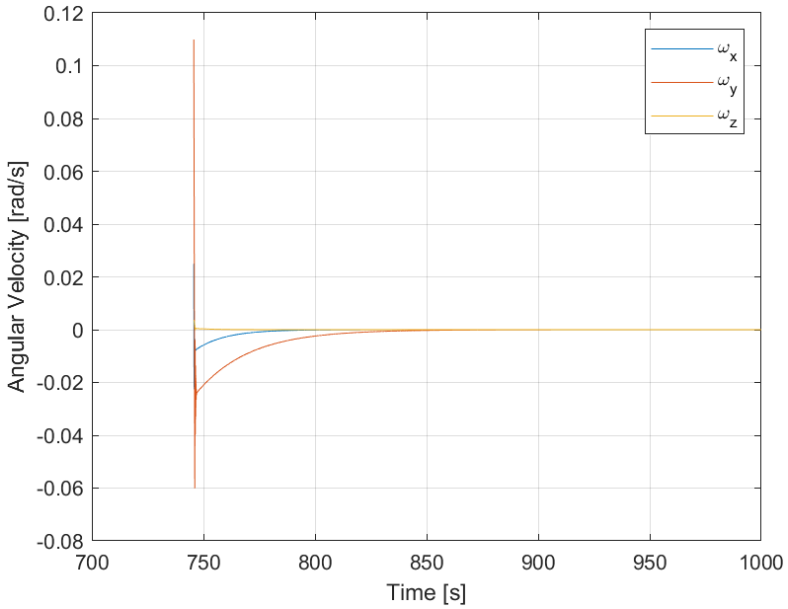

Figure 4.45: Combined system angular velocity during the real approach and docking maneuver.

In the ideal case, the magnetic torque profile is identical for both Sat.1 and Sat.2. However, in this scenario, the magnetic torques are slightly different from one CubeSat to the other due to the effect of the gravity gradient on Sat.2. This can be due to the effect of the gravity gradient on Sat.2, which causes a minimal change in orientation. This small change is enough to make the attitude not perfectly identical and therefore a change in the magnetic torque values arises. Figure 4.46 and Figure 4.47 depict the magnetic torque of the two separate systems.

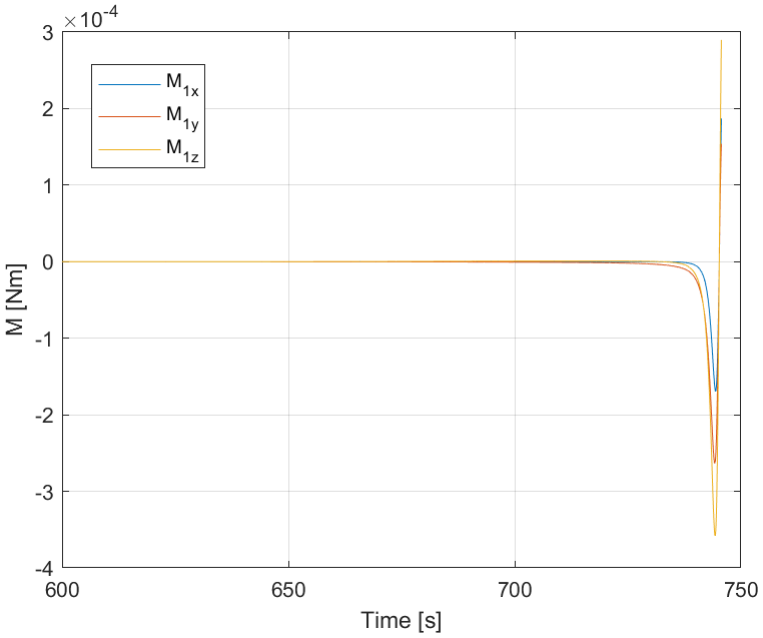

Figure 4.46: Sat.1 angular velocity during the real approach and docking maneuver.

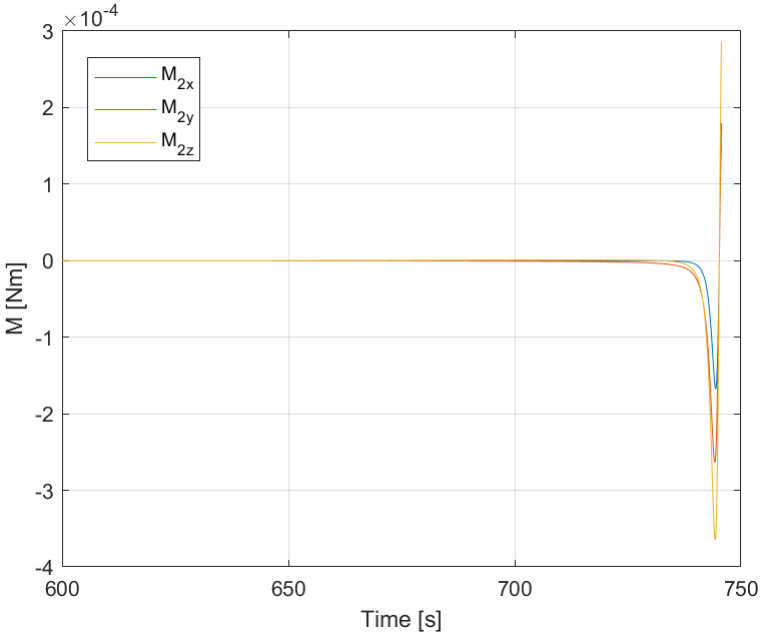

Figure 4.47: Sat.2 angular velocity during the real approach and docking maneuver.

Although the difference between the two graphs is not easily noticeable, the numerical contact value will better highlight the described situation. It can be observed that every component is different from zero. This is attributed to the misalignment between the magnets caused by environmental disturbances and the actions of the controller, resulting in a generated magnetic torque. The contact values are:

$$M_{1c} = (1.869 \cdot 10^{-4},\ 1.540 \cdot 10^{-4},\ 2.897 \cdot 10^{-4})\,[N \cdot m]$$

$$M_{2c} = (1.793 \cdot 10^{-4},\ 1.519 \cdot 10^{-4},\ 2.859 \cdot 10^{-4})\,[N \cdot m]$$

As for previous cases, the magnetic torque value is considered only until contact is achieved. Once the satellites are combined the torque becomes internal to the system and therefore must not be considered further in this analysis.

The main contact characteristics are listed in Table 4.9 to summarize the maneuver and to provide a better overview.

Contact Data for Real Approach and Docking	
Time of contact	$745.6\,[s]$
Contact Position	$r_c = (3.9 \cdot 10^{-3},\ -1.48 \cdot 10^{-2},\ -5.06 \cdot 10^{-3})\,[m]$
Contact Velocity Sat.1	$v_{1c} = (-6.27 \cdot 10^{-3},\ -5.55 \cdot 10^{-4},\ 2.01 \cdot 10^{-3})\,[m/s]$
Contact Velocity Sat.2	$v_{2c} = (-8.71 \cdot 10^{-5},\ 1.51 \cdot 10^{-4},\ -2.38 \cdot 10^{-5})\,[m/s]$
Contact Force Sat.1	$F_{m1_c} = (-1.505 \cdot 10^{-3},\ -2.653 \cdot 10^{-5},\ 9.799 \cdot 10^{-4})\,[N]$
Contact Force Sat.2	$F_{m2_c} = (1.512 \cdot 10^{-3},\ 2.557 \cdot 10^{-5},\ -9.602 \cdot 10^{-4})\,[N]$
Contact Angular Velocity Sat.1	$\omega_{1_c} = (2.511 \cdot 10^{-2},\ 0.110,\ 7.097 \cdot 10^{-3})\,[rad/s]$
Contact Angular Velocity Sat.2	$\omega_{2_c} = (2.492 \cdot 10^{-2},\ 0.109,\ 7.263 \cdot 10^{-3})\,[rad/s]$
Contact Torque Sat.1	$M_{1c} = (1.869 \cdot 10^{-4},\ 1.540 \cdot 10^{-4},\ 2.897 \cdot 10^{-4})\,[N \cdot m]$
Contact Torque Sat.2	$M_{2c} = (1.793 \cdot 10^{-4},\ 1.519 \cdot 10^{-4},\ 2.859 \cdot 10^{-4})\,[N \cdot m]$
Contact Attitude	$q_c = (0.958,\ 0.051,\ 0.279,\ -0.007)$

Table 4.9: Main contact values for the real approach and docking maneuver.

Conclusions

The purpose of this work is to investigate the feasibility and reliability of magnets as the sole mean for small satellites docking. The thesis proposed a contact model to analyze the system before and after contact, which simplifies the design complexity and opens up the possibility for a modular approach to designing larger spacecraft.

This thesis presents the design and development of a MATLAB/Simulink-based simulator for small satellites docking using magnets. The mathematical model employed in the simulation, along with the environmental disturbances that affect the system, were described in detail. The actuation systems and their corresponding model-based control algorithms were also presented, emphasizing the use of an LQR controller for position control and a PD controller for attitude control. At last, the thesis illustrates several test cases for the model, including the initial conditions of the simulations, and presents the resulting outcomes. The analyzed cases are:

- Docking maneuver in ideal conditions;
- Docking maneuver in real conditions;
- Approach and docking maneuver in ideal conditions;
- Approach and docking maneuver in real conditions.

Results for the docking maneuver show that magnets, under a certain relative distance, are a reliable docking mean. The distance at which the magnets are still reliable depends on various factors, i.e. their magnetization and the external disturbances. Additionally, it was observed that the attitude actuation system of one satellite is able to successfully control and stabilize the combined system.

Analyzing results for the final approach and dock maneuver, it was noticed that the addition of the LQR controller provided great benefits in terms of contact energy. In fact, the controlled satellite experiences a drastic reduction in impact velocity compared to the uncontrolled CubeSat, with a difference of two orders of magnitude. Additionally, the position control system of the approaching satellite is capable enough to control the combined system, reaching and maintaining the desired position.

These results demonstrate that magnets could simplify docking maneuvers for small satellites, even in presence of external disturbances. They are a reliable and propellant-free way of achieving contact between spacecraft. The fact that the assembled system can be controlled, opens to the possibility of designing modular spacecraft made, potentially, by several CubeSats. This would be advantageous in terms of both cost and repairability. In fact in the event of a component failure, the modular design enables the replacement of only the affected module, rather than the entire spacecraft. This approach can help to extend the lifespan of the mission and reduce the overall cost of operation.

One of the main challenges of this work has been the accurate estimation of magnetic forces and torques when the magnets are in very close proximity. While the method presented here is functional, it introduces a degree of approximation that could potentially have an impact on the results. Furthermore, in practical applications, it may be necessary to consider the interaction with Earth's variable magnetic field to correctly dimension the attitude actuation system.

To address these issues, future work could involve creating a detailed 3D model of the magnets and studying their interaction to develop a more precise model for this specific scenario. This could potentially involve using advanced simulation tools, i.e. finite element analysis and multi-physics analysis, to analyze the magnetic field generated by the magnets and the resulting forces and torques. In addition, experimental validation of the model could be performed using physical prototypes to ensure the accuracy and reliability of the results. An interesting avenue for future research would be to expand the scope of this work to include simulations of docking scenarios involving multiple satellites. This could help to identify optimal approaching strategies, which could potentially involve formation flight, and inform the design of future small satellite missions.

In summary, this thesis fulfills its objective to demonstrate the feasibility and reliability of magnets as small satellites docking devices. The orbital simulator developed in this work has provided valuable insights into the system behaviour under different conditions. Additionally, the contact characteristics of every considered scenario have been explored. The results of the simulations show that magnets can simplify docking maneuvers for small satellites, even in the presence of external disturbances, and that they are a reliable and propellant-free way of achieving contact between spacecraft. The potential for a future modular approach to spacecraft design using CubeSats is also promising. However, further work is needed to address the challenges associated with accurate magnetic force and torque estimation, as well as to explore multiple satellites scenarios. Overall, this work contributes to the advancement of small satellite technology and opens up new possibilities for future space missions.

Bibliography

[1] John Bowen, Al Tsuda, John Abel, and Marco Villa. «CubeSat Proximity Operations Demonstration (CPOD) mission update». In: *2015 IEEE Aerospace Conference*. 2015, pp. 1–8. DOI: 10.1109/AERO.2015.7119124 (cit. on p. 1).

[2] Miguel Nunes, Trevor Sorensen, and Eric Pilger. «On the development of a 6DoF GNC framework for docking multiple small satellites». In: Jan. 2015. DOI: 10.2514/6.2015-0868 (cit. on p. 1).

[3] Craig Underwood et al. *Autonomous Assembly of a Reconfigurable Space Telescope (AAReST) – A CubeSat/Microsatellite Based Technology Demonstrator*. 2013 (cit. on p. 1).

[4] C Underwood, S Pellegrino, VJ Lappas, C Bridges, and J Baker. *Using CubeSat/micro-satellite technology to demonstrate the autonomous assembly of a reconfigurable space telescope (AAREST)*. 2014 (cit. on p. 1).

[5] J. Pei et al. «Autonomous Rendezvous and Docking of Two 3U CubeSats Using a Novel Permanent-Magnet Docking Mechanism». In: *54th AIAA Aerospace Sciences Meeting*. American Institute of Aeronautics and Astronautics. San Diego, CA, USA, Jan. 2016, p. 1465 (cit. on pp. 1, 15).

[6] Jing Pei. «Ground demonstration on the autonomous docking of two 3U CubeSats using a novel permanent magnet docking mechanism». In: *55th AIAA Aerospace Sciences Meeting*. 2017, p. 0849 (cit. on p. 1).

[7] Luka Skrinjar, Janko Slavič, and Miha Boltežar. «A review of continuous contact-force models in multibody dynamics». In: *International Journal of Mechanical Sciences* 145 (2018), pp. 171–187. ISSN: 0020-7403. DOI: https://doi.org/10.1016/j.ijmecsci.2018.07.010. URL: https://www.sciencedirect.com/science/article/pii/S0020740317333611 (cit. on p. 2).

[8] Hamid Lankarani and Parviz Nikravesh. «A Contact Force Model With Hysteresis Damping for Impact Analysis of Multibody Systems». In: *J. of Mechanical Design* 112 (Sept. 1990), pp. 369–376. DOI: 10.1115/1.2912617 (cit. on p. 2).

[9] Landis Markley and John Crassidis. *Fundamentals of Spacecraft Attitude Determination and Control*. Jan. 2014. ISBN: ISBN: 978-1-4939-0802-8. DOI: 10.1007/978-1-4939-0802-8 (cit. on pp. 4, 12).

[10] N. Bloise, E. Capello, M. Dentis, and E. Punta. «Obstacle Avoidance with Potential Field Applied to a Rendezvous Maneuver». In: *Applied Sciences* 7.10 (2017), p. 1042. DOI: 10.3390/app7101042 (cit. on pp. 5, 27).

[11] Anton H De Ruiter, Christopher Damaren, and James R Forbes. *Spacecraft dynamics and control: an introduction*. John Wiley & Sons, 2012 (cit. on pp. 6, 8).

[12] Elisa Capello, Elisabetta Punta, Fabrizio Dabbene, Giorgio Guglieri, and Roberto Tempo. «Sliding-Mode Control Strategies for Rendezvous and Docking Maneuvers». In: *Journal of Guidance, Control, and Dynamics* 40 (Jan. 2017), pp. 1–8. DOI: 10.2514/1.G001882 (cit. on pp. 8, 21).

[13] VACCO Industries. *VACCO Industries*. https://cubesat-propulsion.com/standard-micro-propulsion-system/. [Online; accessed 22-March-2023]. 2023 (cit. on p. 22).

[14] Hyungjoo Yoon, Hyun Ho Seo, and Hong-Taek Choi. «Optimal uses of reaction wheels in the pyramid configuration using a new minimum infinity-norm solution». In: *Aerospace Science and Technology* 39 (2014), pp. 109–119. ISSN: 1270-9638. DOI: https://doi.org/10.1016/j.ast.2014.09.002. URL: https://www.sciencedirect.com/science/article/pii/S1270963814001734 (cit. on p. 25).